Electrical Properties Tomography Based on B_1 Maps in MRI: Principles, Applications and Challenges

Jiaen Liu,

Advanced MRI Section, Laboratory of Functional and Molecular Imaging, National Institute of Neurological Disorders and Stroke, National Institutes of Health, Bethesda, Maryland, 20892, USA

Yicun Wang,

Department of Biomedical Engineering, University of Minnesota, Minnesota, 55455, USA

Ulrich Katscher, and

Philips Research Europe, Hamburg, 22335, Germany

Bin He[*] **[Fellow, IEEE]**

Department of Biomedical Engineering and Institute for Engineering in Medicine, University of Minnesota, Minnesota, 55455, USA

Abstract

Electrical properties (EPs), including conductivity and permittivity, are closely related to many fundamental properties of tissue and its pathological conditions. Noninvasively measuring the *in vivo* EPs of tissue can have an important impact on biomedical research and clinical applications. Among approaches developed for EP quantification and imaging, electrical properties tomography (EPT) is a promising technology that reconstructs EPs based on the B_1 field distribution that can be measured in the radiofrequency range using an MRI device. In this article, we review the basic principle of EPT, reconstruction methods, biomedical applications including tumor imaging, and existing challenges. As an important application of EPT, the estimation of specific absorption rate (SAR) and its current development are discussed.

Index Terms

electrical properties; B_1-mapping; electrical properties tomography; EPT; magnetic resonance imaging; MRI; Quantitative magnetic resonance imaging

I. Introduction

Electrical properties (EPs), also known as dielectric properties, including electrical conductivity (σ) and permittivity (ε), are fundamental properties of materials. Conductivity

Bin He: binhe@umn.edu.

characterizes the capability to transfer electrical current inside the medium. Permittivity is directly related to the effect of electric polarization that happens when the electric charges of molecules separate to counteract the external electric field. In biological tissues, EPs are determined by the fundamental biophysical properties of the tissue, such as water content, ion concentration, molecular composition, fraction of intracellular space, permeability of the cell membrane, cellular structure, etc.[1]–[5] A unique frequency-dependent characteristic of biological EPs has been observed, with three major stages, also known as dispersions, at various frequencies [6]. This frequency dependency was explained in part by the nonconductive nature of cell membrane at low frequency and by the phenomenon of dielectric relaxation that happens on electrically polarized molecules – such as water and protein – and structures such as cell membrane in a time-varying electromagnetic field [4]. The frequency spectrum of biological EPs can be described by relaxation models with multiple relaxation time constants to incorporate various dispersions. These models include variants of Debye [3] or Cole-Cole [7] equations.

Electrical properties can potentially be used as biomarkers indicating the healthiness condition of tissue in clinical applications. Previous non-MRI-based (MRI: magnetic resonance imaging) studies have shown that various diseases cause local changes of EPs relative to the healthy nearby tissue. Among various cancers, breast cancerous tissue has been shown with the most different EPs compared to normal breast tissue [8], [9]. Benign breast tissue shows significantly different conductivity compared to malignant breast carcinoma [10]. Studies showed that cerebral ischemia could decrease conductivity up to 60% [11], [12], suggesting an effective method for differentiating ischemic and hemorrhagic stroke. Local ischemia and cell swelling that happen due to a focal seizure during epilepsy can also change the electrical properties [13].

Tissue EPs play an important role in biomedical research. They are useful for understanding the distribution of electromagnetic field inside tissue. For example, accurate EP models are needed to localize the internal electrical activities based on noninvasive electrophysiological recording over the body surface such as electroencephalography (EEG) [14]–[19] and electrocardiography (ECG) [20]–[24]. On the other hand, EPs are critical to estimate the distribution of electric current and electromagnetic power inside the body in applications utilizing electromagnetic stimulation for treatment, such as deep brain stimulation (DBS) to mitigate Parkinson's disease symptom [25]–[27], transcranial direct current stimulation [28], transcranial magnetic stimulation (TMS) in neuropsychiatry [29], radiofrequency (RF) ablation to remove arrhythmic genesis foci [30] and RF hyperthermia in cancer treatment [31]. EP model of the body is also critical to quantify tissue heating induced by electromagnetic wave used in cell phones or MRI.

In the past decades, much effort has been made to map distribution of tissue EPs *in vivo*. Among related techniques, electrical impedance tomography (EIT) [32]–[36] has been well explored and developed to provide high temporal resolution. However, EIT requires mounting electrodes and injecting current into the sample but provides limited spatial resolution due to the ill-posed nature of the inverse problem. Magnetic resonance electrical impedance tomography (MREIT) [37]–[45] utilizes MRI to detect the magnetic field induced by the probing current, providing high spatial resolution, but requires safety-

concerning current density to reach a sufficient signal-to-noise ratio (SNR) within an MRI scanner. Instead of injecting electrical current from surface electrodes which may suffer from the shielding effect of non-conductive tissue, magneto-acoustic tomography with magnetic induction (MAT-MI) was proposed [46], which uses magnetic induction and ultrasound measurement to obtain high spatial resolution [46]–[49]. However, what remains to be improved is the limited contrast in MAT-MI images due to electromagnetic interference.

Recently, electrical properties tomography (EPT) was introduced as a non-invasive *in vivo* imaging approach to simultaneously map conductivity and permittivity at the resonant frequency of water proton using MRI [50]–[53]. As shown in Fig. 1, three-dimensional distribution of EPs can be reconstructed from measured maps of B_1 field (also referred to as RF field) inside the sample. During an MRI scan, the B_1 field is generated on an RF transmitting device (commonly known as an RF coil) for generating signals carrying information about the water protons in the body. The B_1 field can be quantitatively mapped throughout the sample utilizing B_1-mapping techniques. EPT reconstruction algorithms are developed based on the Maxwell's equations, which address the distribution of electromagnetic field as a function of EP distribution in the sample. In principle, EPs can be reconstructed either voxel by voxel considering the distribution of B_1 field within a voxel's neighboring region or globally inside an entire volume utilizing global B_1 information. EPT can achieve high spatial resolution and deep penetration depth without surface electrodes or current injection. An EPT scan is conducted similarly to existing MRI techniques, making it potentially applicable for clinical applications.

Sections II and III introduce the principle of EPT and review its reconstruction algorithms and corresponding experiment setups, respectively. Section IV provides a survey of the applications of EPT in which EPs were used as an imaging contrast to characterize diseased tissues.

Tissue heating due to power absorption from the applied RF field during an MRI scan is a safety concern and limiting factor for the development of high field MRI. Based on current standard (International Standard IEC 60601-2-33 2010), tissue heating is measured by the quantity of specific absorption rate (SAR), which must be estimated before scanning. Today's MR scanners usually apply generic human models for local SAR determination, requiring large safety margins to account for potential deviations between the model and individual subjects. Optimally, local SAR would be estimated by a realistic, high resolution model based on *in situ* measurements of the individual subject, but the intimidating efforts required to set up such models currently prohibits their use in clinical routine. Moreover, an accurate SAR estimation requires modelling the involved transmit coil not in its ideal status but its operating status. Particularly for transmit arrays, which are promising for addressing B_1 intensity variation at high fields (3 T or above) [54], [55], actual and ideal coil status might differ by loading effects, decoupling issues, dysfunction of single transmit channels, etc.

As an alternative to model-based SAR estimation, it was suggested to estimate SAR in the framework of EPT, i.e., by post-processing (complex) B_1 maps as shown in Fig. 1. EPT-

based SAR determination automatically includes the individual subject and the operating status of the transmit channel(s), overcoming corresponding problems of model-based SAR estimation and useful for designing the optimal B_1 field for the individual subject. Thus, aside from diagnostic applications, EPT can play an important role in the framework of RF safety management. Section V outlines the background of EPT-based SAR determination and gives an overview of corresponding studies reported.

II. Basic Principles of MR-based EPT

In this section, the concept of EPT will be introduced, the instrumental mechanism of measuring the B_1 field using MRI for EPT reconstruction will be briefly reviewed, and the core equations deducing various reconstruction algorithms will be presented. Studies on anisotropic EPs are beyond the scope of this review.

A. Relationship Between EPs and B_1 Field

MRI employs a strong static magnetic field (B_0 field) and the time-varying B_1 field at the Larmor frequency to induce precession of the nuclear spins — of water proton within the scope of this review — about the direction of B_0. In the view of classical mechanics, the assemble of spins can be represented by a vector of magnetization that is originally aligned with B_0 and precesses about B_0 after the RF excitation. The RF signal generated by the magnetization precession can be detected by receive RF coils.

The relationship between the distribution of the B_1 field and the underlying EPs of the sample is governed by Maxwell's equations [56], [57]. Faraday's Law and Ampère's Law in Maxwell's equations describe the interactive relationship between the time-varying magnetic and electric field in a medium with a specific distribution of EPs and magnetic permeability (μ). Because the frequency spectrum of the applied B_1 field is usually closely centered at the precessing frequency of the nuclear spins, the field can reasonably be treated to be time harmonic, i.e. oscillating at a single frequency. The time harmonic forms of Faraday's Law and Ampère's Law are

$$\nabla \times \mathbf{E}(\mathbf{r}) = -j\omega \mathbf{B}(\mathbf{r}) \quad (1)$$

and

$$\nabla \times \mathbf{B}(\mathbf{r}) = j\omega\mu\varepsilon_c \mathbf{E}(\mathbf{r}), \quad (2)$$

respectively. Here, $\mathbf{B}(\mathbf{r})$ and $\mathbf{E}(\mathbf{r})$ denote the spatially dependent component of the magnetic and electric field, respectively, in the Cartesian coordinate, $\varepsilon_c := \varepsilon - i\dfrac{\sigma}{\omega}$ is known as the complex permittivity, $\mathbf{r}$ represents location and ω the oscillating angular frequency of the fields. In the rest of the paper, $\mathbf{r}$ will be eliminated since the derivatives only take place in space in the equations. Taking the curl operation on both sides of (2) and combining the

result with (1), the relationship between **B** and the electromagnetic properties of the medium is

$$-\nabla^2\mathbf{B}=\omega^2\varepsilon_c\mu_0\mathbf{B}+\nabla\varepsilon_c\times\frac{\nabla\times\mathbf{B}}{\varepsilon_c} \quad (3)$$

where μ of tissue has been assumed to be equal to μ_0 of the free space.

To be able to estimate EPs from MR images, the signals generating the images should carry some form of information about the B_1 field. In general, the signals from a voxel in the sample induced by the transmit RF pulse and picked by a receive RF coil can be expressed as [58]

$$S=\rho C\sin(\alpha)e^{i\arg(B_1^+)}B_1^{-*} \quad (4)$$

where B_1^+ is traditionally known as the transmit B_1 field inducing the precession of the magnetization, B_1^- is the sensitivity of the RF coil to pick up the MR signals, also known as the receive B_1 field, arg() denotes the phase of a complex number, '*' indicates complex conjugate, α the angle between B_0 and the magnetization after RF excitation (also known as the flip angle), ρ is the density of water protons and C represents a contrast term due to a combination of factors underlying an MR image, such as T1 and T2 relaxation, flip angle, etc. To accurately map α, C can either be designed to be insensitive to α [59] or manipulated to be sensitive to α in a specific fashion [60], [61].

Equation (4) shows that the MR signal is proportional to the sinusoid of flip angle and magnitude of B_1^-, and the signal is complex with its phase including the transceive phase, which is the sum of the phases of B_1^+ and B_1^{-*}. As a matter of fact, B_1^+ and B_1^- are the components of the B_1 field in the axial plane viewed in the positive and negative rotating frames, respectively [58]. The transformation from B_1^+ and B_1^- in the rotating frames to B_x and B_y in the Cartesian frame can be formulated as [58]

$$\begin{cases} B_1^+=(B_x+iB_y)/2 \\ B_1^-=(B_x-iB_y)^*/2 \end{cases} \quad (5)$$

which together with Gauss's Law $\nabla\cdot\mathbf{B}=0$ enables establishing the relationship between EPs and the MRI-visible B_1^+ and B_1^- as [62], [63]

$$-\nabla^2 B_1^+ = \omega^2 \varepsilon_c \mu_0 B_1^+ - \left(\frac{\partial B_1^+}{\partial x} - i \frac{\partial B_1^+}{\partial y} + \frac{1}{2} \frac{\partial B_z}{\partial z} \right) (g_x + i g_y) - \left(\frac{\partial B_1^+}{\partial z} - \frac{1}{2} \frac{\partial B_z}{\partial x} - i \frac{1}{2} \frac{\partial B_z}{\partial y} \right) g_z$$

(6)

and

$$-\nabla^2 B_1^{-*} = \omega^2 \varepsilon_c \mu_0 B_1^{-*} - \left(\frac{\partial B_1^{-*}}{\partial x} + i \frac{\partial B_1^{-*}}{\partial y} + \frac{1}{2} \frac{\partial B_z}{\partial z} \right) (g_x - i g_y) - \left(\frac{\partial B_1^{-*}}{\partial z} - \frac{1}{2} \frac{\partial B_z}{\partial x} + i \frac{1}{2} \frac{\partial B_z}{\partial y} \right) g_z$$

(7)

where $\mathbf{g} := (g_x, g_y, g_z) := \nabla \ln \varepsilon_c$. Equations (6) and (7) serve as the cornerstone to estimate EPs from measured B_1 information. It should be noted that the B_z component lies in the same direction as the B_0 field and on the scale of 10^{-6} the latter. So B_z does not contribute to MR signals significantly enough that it can be detected based on current MRI methods. For RF coils, of which the conductors are oriented in parallel with the B_0 direction, B_z can reasonably be assumed to be zero, and then, (6) and (7) become

$$-\nabla^2 B_1^+ = \omega^2 \varepsilon_c \mu_0 B_1^+ - \left(\frac{\partial B_1^+}{\partial x} - i \frac{\partial B_1^+}{\partial y} \right) (g_x + i g_y) - \frac{\partial B_1^+}{\partial z} g_z$$

(8)

and

$$-\nabla^2 B_1^{-*} = \omega^2 \varepsilon_c \mu_0 B_1^{-*} - \left(\frac{\partial B_1^{-*}}{\partial x} + i \frac{\partial B_1^{-*}}{\partial y} \right) (g_x - i g_y) - \frac{\partial B_1^{-*}}{\partial z} g_z$$

(9)

.

Assuming the distribution of EPs is smooth so that the gradient term $\mathbf{g}$ can be ignored, (6) and (7) can be simplified into the Helmholtz equations as

$$-\nabla^2 B_1^+ = \omega^2 \varepsilon_c \mu_0 B_1^+$$

(10)

and

$$-\nabla^2 B_1^{-*} = \omega^2 \varepsilon_c \mu_0 B_1^{-*}$$

(11)

where it shows that in homogeneous regions, EPs are solely determined by the distribution of the B_1 components in the xy-plane which are in the MR-signal equation (4).

B. B_1-mapping

Equations (8) and (9) suggest that once the complex B_1 field is mapped, EP distribution can be reconstructed. Conventionally, the so-called B_1-mapping technique refers only to the measurement of the distribution of $\left|B_1^+\right|$ based on acquired MR images, but in the context of EPT reconstruction, both the magnitude and phase of B_1^+ or B_1^- are relevant. A comprehensive review of different B_1-mapping techniques is beyond the scope of this paper. In the following, only a few examples will be discussed to provide some basic ideas.

Since $\left|B_1^+\right|$ is proportional to the induced flip angle α, one strategy for mapping $\left|B_1^+\right|$ is to measure the distribution of α. Note that this linear relationship is normally valid because the RF pulse duration τ is much shorter than the T2* and T1 relaxation time of most tissues. For example, α can be calculated from the division of signals of two scans to eliminate other confounding factors, with α of one scan to be twice as much as that of the other and a long TR to minimize the dependency of C in (4) on α [59]. Another example of α-based B_1 mapping is the so called actual flip angle imaging (AFI) [60], which exploits the signals from two alternating steady states established with two alternating TRs; the ratio of the signals or Cs in the two states is a function of α and the ratio of TRs. In a more recent paper, a technique dubbed "dual refocusing echo acquisition mode" (DREAM) was proposed to calculate α based on the signals of stimulated echoes and free induction decay [61].

With the Bloch-Siegert shift-based approach, the phase of MR signals is utilized to derive $\left|B_1^+\right|$ when an off-resonance RF pulse, whose central frequency deviates from the Larmor frequency of the B_0 field, induces a phase accumulation proportional to the square of $\left|B_1^+\right|$ [64], [65]. When the off-resonance frequency is significantly large, this relationship approximates to be linear. Two scans with symmetric off-resonance frequency shifts can be used to acquire the B_1-related phase signal for estimating $\left|B_1^+\right|$.

III. Reconstruction Methods

Methods for solving the EPT problem can generally be divided into local and global approaches. As shown in Fig. 2a, with the local solution, the measured B_1 data in the voxels about a specific location is used to calculate the EPs at that location. The relationship of EPs between neighboring voxels is not utilized. On the other hand, the global solution is derived from measured B_1 data within the entire region of interest (ROI) as shown in Fig. 2b, and the inter-voxel relationship of EPs is utilized either based on Maxwell's equations or by introducing certain regularization strategies to improve the image quality.

In addition, among global solutions, methods can be categorized based on the direction of the calculation into forward and backward solutions. Employing a forward solution, the B_1 field is updated iteratively by reducing the difference between the measured B_1 data and the

derived B_1 distribution which is based on the calculated EPs, whereas a backward solution only involves calculation of EPs from the measured B_1 data.

A. Local Solutions

A.1. Helmholtz-based Methods Using a Birdcage RF Coil—In clinical MRI setups at 1.5 or 3 T, the quadrature birdcage coil is the most commonly used transmit device due to its uniform B_1^+ coverage [66]. When the birdcage coil is used for transmitting and receiving, the absolute B_1^+ phase of the RF transmitter and the B_1^{-*} phase of the receiver are approximately equal ("transceive-phase assumption", TPA) as shown in Fig. 3a [51], [52], [67], [68]. Based on this empirical observation, the absolute B_1^+ phase can be estimated as half of the transceive phase after other phase contributions from off-resonance effect are removed. In Fig. 3b, the idea of quantitative estimation of absolute B_1 phase using B_1 information from multiple RF channels is illustrated and will be discussed in detail in Section A.2.

As can be seen in the Helmholtz equations (10) or (11), assuming a locally homogenous EP distribution ("local homogeneity assumption", LHA), EP value on each voxel can simply be calculated locally with obtained maps of the transverse B_1 field components B_1^+ or B_1^{-*} without the necessity of any assumptions about B_z. Using a birdcage transceive RF coil and TPA, a local EPT solution is readily available. This approach has been adopted in some early EPT works [50]–[52], [67], [68].

It has been suggested that in the frequency range corresponding to MR field strength below 3 T, where the wave behavior of B_1 is less significant, the absolute B_1 phase depends on the conductivity distribution more than the permittivity while permittivity is more closely related to the magnitude of B_1 fields [51], [67], [68]. Based on this observation, a phase-only conductivity reconstruction and a magnitude-only permittivity reconstruction method have been proposed as

$$\sigma \approx \frac{\nabla^2 \varphi^{\pm}}{\mu\omega} = \frac{\nabla^2 \varphi}{2\mu\omega} \quad (12)$$

and

$$\varepsilon \approx -\frac{\nabla^2 \left| B_1^{\pm} \right|}{\mu\omega^2 \left| B_1^{\pm} \right|} \quad (13)$$

where φ^+ and φ^- are the absolute phase of B_1^+ and B_1^{-*}, respectively and $\varphi := \varphi^+ + \varphi^-$ is the transceive phase. The phase-only conductivity reconstruction is interesting because acquisition of phase data does not require additional B_1-mapping procedures. Spin-echo [52], zero-echo-time [69] or steady-state-free-precession (SSFP) [70] sequences are less sensitive to background B_0 distortion or chemical shift. The transceive phase can be

estimated from such data without acquiring an additional B_0 map, leading to reduced scanning time [70], [71].

Figure 4 exhibits results of EPs using the LHA with magnitude $\left|B_1^+\right|$ and TPA-estimated phase φ^+ (Figs. 4c and d) [67]. This first *in vivo* study of EPT demonstrated its application for brain imaging based on LHA and TPA. The reconstructed conductivity shows reasonable value and colocalization with the gray/white matter and cerebrospinal fluid (CSF), while the permittivity result has a more severe problem, such as deviated anatomy compared with the reference MRI (Fig. 4b) and unrealistic values ($> 200 \ \varepsilon_0$) particularly along the rim of the brain. This could be due to the large kernel size of the calculus operations smearing over different compartments [67].

The effectiveness of the introduced local solution so far can be challenged by several factors:

First of all, due to the violation against LHA, errors can happen near the interface between regions of different EP value [72], [73]. Tissues are usually characterized by complicated branching/frayed/fringed/fringy structures and thus spatially varying EP distribution. One way of improving the reconstruction near boundaries is to constrain the Laplacian operator within a region of ideally uniform EP value based on some reference image [67], [74], [75]. In practice, interpretation of the results using this strategy calls for caution because the reference image can potentially lead to bias in the EP reconstruction. Another approach is to use inhomogeneous equations such as (8) and (9) to construct the reconstruction algorithm. Using (8) and (9), the spatial gradient of $\ln \varepsilon_c$ can be calculated to improve the reconstruction near boundaries [53], [63], [76]–[78]. This approach will be discussed later.

Secondly, the assumption of TPA becomes increasingly invalid at high field strength or with a non-quadrature RF coil. Increased field strength holds promises for improved intrinsic SNR and introduces more significant wave effect beneficial for EPT reconstruction. Moreover, high field MRI applications call for more accurate SAR estimation based on individual EP model and the current status of the RF-transmitting device [62], [79], [80]. At high (3 T) and ultrahigh (7 T) field, non-quadrature RF coils such as multi-channel parallel transmit RF coils or phased-array receive coils are beneficial for improved excitation coverage, SNR and accelerated acquisition [54], [55], [81]–[85].

Van Lier et al. in 2013 has investigated the validity of the TPA assumption and phase-only conductivity reconstruction using quadrature birdcages RF coils at 1.5, 3 and 7 T, respectively. As shown in Fig. 5, the TPA assumption remains reasonably accurate at 1.5 and 3 T while introduces apparent phase error towards the peripheral of the head model and conductivity error in the phantom experiment and simulation both at 7 T. The conductivity estimation is even more severely disrupted if phase-only reconstruction is carried out.

Thirdly, local solutions are sensitive to noise in the measured B_1 data and modeling errors. The effect of these error sources can be amplified through the Laplacian operator ∇^2 in equations (8) and (9). Laplacian operation is effectively a high-pass spatial filter, and it amplifies spatial frequency harmonics to the second order of their frequency. To reduce the noise effect, a low-pass spatial filter can be applied on the B_1 data before any reconstruction

calculation. The resultant SNR of the reconstructed EPs is proportional to the square of the linear dimension of the effective kernel, which combines the Laplacian and the low-pass filter, and the square root of the number of voxels in the kernel [86]. However, using a low-pass filter will compromise the effective resolution. As will be discussed later in Section III.B, a global solution is helpful to reduce noise sensitivity of the local EPT algorithms without relying on a strong low-pass filter.

A.2. Local solutions Using Multi-channel B₁ maps—The need for quantitatively calculating absolute B_1 phase without relying on TPA or calculating EPs and their gradient using the inhomogeneous equations (8) and/or (9) motivates using multiple channels of RF elements to collect B_1 data to solve for the additional unknowns. Fig. 3b is demonstrated as an example in which the magnitude of $\left|B_1^+\right|$ or $\left|B_1^{-*}\right|$ and the corresponding relative phase between different channels are acquired for calculating the unknown absolute phase of B_1^+ or B_1^{-*} of a reference channel [63], [87]–[89]. In addition, the transceive phase of a pair of transmit and receive channels can be obtained and used to solve the common unknowns, including EPs and absolute B_1 phase [76], [90]–[92]. Note that $\left|B_1^{-*}\right|$ measurement is usually weighted by the unknown proton density ρ in the form of $\left|\rho B_1^{-*}\right|$. Later, methods eliminating the effect of ρ will be discussed.

In [87], an equation about B_1^+ and B_1^{-*} was derived based on the Gauss' Law for magnetism and used to calculate absolute phase using measured relative phase and magnitude data. This approach requires that B_1^+ and B_1^{-*} come from the same RF channel, and therefore, it is critical to accurately quantify any additional phase delay on the transmit or receive line and rescale the magnitude of $\left|B_1^+\right|$ and $\left|B_1^{-*}\right|$ on each channel based on a calibration. The works in [88], [90], [91] were based on the Helmholtz equations (10) and/or (11) using the relative and/or transceive phase data. In [89], a reconstruction algorithm was developed based on (11) and the relative sensitivity data of receive B_1 channels. Relative receive sensitivity is inherently insensitive to non-B_1^{-*}-related components in the signal equation (4) such as T1, proton density and B_1^+. Additionally, it can be acquired efficiently with a single RF excitation. However, the concept is so far only implementable based on the Helmholtz equation, causing boundary errors, and the result can be sensitive to noise effect because the method relies on a third-order derivative to calculate EPs.

Based on the inhomogeneous equations (8) and (9), using multi-channel $\left|B_1^+\right|$, $\left|\rho B_1^{-*}\right|$ and relative phase of B_1^+ and B_1^{-*}, a gradient-based EPT method was proposed to first calculate a local solution of EP gradient and then obtain the final EP maps by integrating the gradient [63]. A typical result of brain EPT imaging is shown in Fig. 6. Because integration reduces high frequency noise, the result features enhanced robustness against noise contamination. The details of brain structure as revealed in the T1-weighted anatomical image can also be visualized in the images of conductivity and permittivity without disruptive error near boundaries between different tissues. The nominal in-plane resolution was 1.5 mm. With applied Gaussian filter, the effective resolution was around 5 mm. This work demonstrated

the capability of EPT to achieve high resolution images of human brain *in vivo*. When B_1^{-*} is considered, the unknown ρ needs to be first removed. In this and earlier studies [87], [90], ρ was extracted based on the symmetric pattern of B_1^+ and B_1^{-*}. It was shown later that, with measured transceive phase, ρ can be reconstructed quantitatively based on the transmit and receive B_1 data [76]. In another study [92], it was suggested in theory that with sufficient B_1 data, including magnitude, relative and transceive phase, and sufficient number of independent RF elements, a full model can be established to reconstruct absolute B_1 phase, EPs and ρ, even without assuming $B_z=0$. However, this model remains to be demonstrated to be feasible in practice due to its high numerical complexity and adverse noise figure.

B. Global Solutions

Although the local solutions are straightforward to conceive and implement, they ignore the relations of EPs on neighboring voxels. As mentioned earlier, noise in the B_1 data is amplified through the Laplacian operator ∇^2. Solving the EPT reconstruction problem essentially derives a solution of partial differential equations (PDE) about EPs and B_1 field. As shown in Fig. 2, in calculating a global solution, the B_1 data from the entire ROI is provided to the solver, and EPs in all the voxels in the ROI are obtained together instead of one voxel after another. The relationship of EPs between neighboring voxels is automatically considered in the model. The aforementioned gradient-based EPT can be considered as a hybrid method, with a local solution of gradient and global solution of final EPs based on the calculated gradient.

A global EP solution can be obtained based on backward calculation from the measured B_1 data to reconstructed EP values. This approach was first realized in the so-called crMREPT method [77]. Replacing $\dfrac{1}{\varepsilon_c}$ with λ, equation (8) is transformed to a linear PDE [77], [78]

$$-\omega^2\mu_0 B_1^+ = \left(\frac{\partial B_1^+}{\partial x} - i\frac{\partial B_1^+}{\partial y}\right)\left(\frac{\partial \lambda}{\partial x} + i\frac{\partial \lambda}{\partial y}\right) + \frac{\partial B_1^+}{\partial z} \cdot \frac{\partial \lambda}{\partial z} + \nabla^2 B_1^+ \lambda \tag{14}$$

.

In the crMREPT study, λ was calculated globally based on a measured transmit B_1 magnitude and TPA-estimated absolute transmit B_1 phase using the finite-element method. From the same group, a phase-only gradient-based global solution of conductivity has been proposed derived from (14) [78].

As shown in Fig. 7, we used simulated B_1^+ data based on finite-difference time-domain (FDTD) method to demonstrate the effect of noise on an example of global solution in comparison with a local solution. Complex B_1^+ from sixteen channels of the RF array coil was generated with a homogeneous cylindrical dielectric model with isotropic 2-mm resolution. Gaussian noise was added to the real and imaginary parts of B_1^+ with a spatially constant standard deviation (SD). SD was 1/SNR times the average $\left|B_1^+\right|$ in the dielectric

model. The noise-contaminated data was first filtered with a 3D low-pass Gaussian filter with a standard deviation of σ_{Gaussian}. The global solution was constructed based on (14) and the finite-difference method [93] within a xy-plane, with eliminated $\dfrac{\partial B_1^+}{\partial z} \cdot \dfrac{\partial \lambda}{\partial z}$ and using the noise-contaminated sixteen B_1^+ data sets. The local solution was calculated based on (10) using the same B_1^+ data. Note that since the model is homogeneous, using the Helmholtz equation (10) is justified. In Figs. 7a and 7b (SNR=100), it can be observed that the results using the global solution show less fluctuating profiles compared to the local solution results, with the latter swinging about the target value of the simulation input and the former globally biased. At a lower SNR of 50, using the same σ_{Gaussian} as that in Figs. 7a and 7b, both the fluctuation of the local solution and global bias of the global solution become more significant as shown in Figs. 7c and 7d, especially near the center of the model. Increasing σ_{Gaussian} of the filter removes a larger portion of the random noise and improves the performance of the both methods as shown in Figs. 7e and 7f. In general, it can be observed that the global solution can significantly reduce the fluctuating effect of the noise because the relationship of EPs between neighbor voxels are used as additional information to reduce the Laplacian-and-derivative amplified noise fluctuation. However, the global solution has the side effect of a systematical global bias around the center of the model. In this example, B_1^+ data from all the channels tends to have a very low magnitude of $\left| \dfrac{\partial B_1^+}{\partial x} - i\dfrac{\partial B_1^+}{\partial y} \right|$ around the center, reducing the efficacy of the global solution around the central region. A similar problem has been observed in the crMREPT study, in which artifacts arise around the region with low $\left| \dfrac{\partial B_1^+}{\partial x} - i\dfrac{\partial B_1^+}{\partial y} \right|$.

A global solution can also be derived based on a forward model in which the complex B_1 distribution is calculated for specific EPs with a RF coil model or certain boundary conditions about B_1; the EP solution is updated iteratively to minimize the difference between calculated B_1 distribution in the forward model and the measured B_1 data. In the contrast source inversion (CSI) EPT study [94], the total field was modeled as the sum of the incident field in an empty coil and the secondary scattered field when the coil is loaded with the object. This method does not need any assumption about B_z distribution. However, accurate forward calculation of the incident magnetic and electric field with an accurate model of the RF coil and consideration of scattering effect inside the MR bore is quite challenging. Another similar approach that was also formulated based on the scattering theory can be found in [95]. In the study of [96], the dubbed global maxwell tomography method iteratively reconstructs EPs based on a full model of the RF coil and the subject until the simulated $\left| B_1^+ \right|$ is sufficiently close to the measured map. It faces the similar challenge of the demanding modelling accuracy as the CSI-EPT method. Instead of a full model of the RF coil, in [97], forward calculation of B_1^+ was based on (8) and simulated B_1^+ (or measured data in experiment) on boundary of the ROI assuming B_z=0.

Global solution can be constructed by introducing regularization methods to improve the image quality which can be hampered by the intrinsic limitation of EPT, such as noise amplification, missing B_1 components, violation of LHA, etc. In the CSI-EPT method, improved robustness against noise was shown using a multiplicative total variance regularizer. In a recent work [98], different regularization strategies were applied to regions of smooth EP distribution and regions of rapid EP changes, respectively, with the former aimed at reducing amplification of random noise and modeling error and the latter preserving the edge of tissue EPs. In contrast to the global methods which rely on the inhomogeneous equations such as (8) or (14), formulations utilizing the simplified, LHA-based equations such as (12) and regularization schemes have been proposed and shown with improved performance near boundaries and reduced sensitivity to noise [99], [100].

C. Spatial and Temporal Resolutions

In an ideal situation when the B_1 data is free of thermal noise, spatial resolution of the reconstructed EP image using EPT depends on the resolution of the measured B_1 map, preprocessing method and reconstruction algorithm. In a previous study [76], profiles of the reconstructed EPs using the full equations (8) and (9) and simulated noise-free B_1 data suggest the same resolution of the reconstruction as the input B_1 data. In practice, when a low-pass filter is used to reduce the noise effect, the effective resolution will depend on the filter. For example, a Gaussian filter with a standard deviation of σ_g voxels will result in an effective resolution of 2.67 σ_g based on the full width of half maximum (FWHM) of the Fourier spectrum of the filter [63]. The level of smoothing is driven by the desired contrast-to-noise ratio (CNR) in the reconstructed EPs. Analysis of the noise level in the reconstructed EPs suggests that it is related to the field strength, FWHM (in unit of length rather than voxels) of the low-pass filter and number of measured voxels in the kernel of low-pass filter and Laplacian [86]. By considering the integrative effect of these factors, so far a resolution between 3 and 5 mm has been achieved in the reconstructed EP image [63], [101], [102].

Temporal resolution of EPT methods varies as the B_1 data required for different reconstruction algorithms differs. The phase-based conductivity reconstruction based on (12) or proposed in [78] only utilizes the transceive phase which can be acquired with a fast, B_0-insensitive SSFP sequence. A time frame of 4 s of conductivity imaging based on (12) has been reported [70]. The approach [89] based on the relative coil sensitivity also has the advantage of a high temporal resolution even though the original paper was published using the data acquired with a slower GRE sequence.

IV. Biomedical Applications of EPT

A. Cancer diagnosis, staging and grading

Tumorigenesis is accompanied by significant local changes at molecular, cellular and tissue levels. For example, sodium concentration and water content are elevated due to aggressive proliferation; nucleus takes a much larger volume of the cell body and cytoplasm becomes much denser; cellular density substantially increases with extracellular matrix impaired to facilitate cancer invasion. These abnormalities also develop as tumor grows into various

stages. EPs, as fundamental physical properties of biological tissues, correlate with the tumor features and represent responsible and responsive indicators for cancer diagnosis, staging, and grading.

It is noteworthy that a huge variation of tissue EPs exists across the body, such that contrast between normal and cancerous tissue is dependent not only on tumor itself but also the properties of its surrounding tissues [9]. This heterogeneity of contrast plays a fundamental role when determining the sensitivity and specificity of EPT to pinpoint cancer in different organs.

A.1 Breast Cancer—Utilizing different implementations of the polynomial fitting method of turbo spin echo or fast spin echo phase maps, several pilot studies have demonstrated significant conductivity elevation in malignant lesions compared to normal breast tissues and benign cysts [74], [103], [104]. A retrospective study involving 65 female patients with invasive breast cancer further revealed the correlation between reconstructed conductivity and prognostic information such as tumor type and status [105]. The clinical applicability of EPT is still pending establishment, potentially through large-scale prospective studies including various subtypes, sizes, and stages of breast lesions.

A.2 Other Cancer Types—EPT can also be applied to examine other organs for cancer characterization. As shown in Fig. 8a, in the pelvis, feasibility of conductivity measurement in cervix tumor has been demonstrated in 20 patients [106], [107]. In the brain, conductivity of glioma has been reported to deviate from surrounding healthy tissue [108], [109]. This deviation varies with tumor type and positively correlates with tumor grade, which is important reference information for therapy design, and was reported to be consistent with probe measurements of excised specimen [110], [111].

A.2 Animal Cancer Models—Recently, tumor-bearing rodent models have been used in several EPT studies. Animal models have the unique advantages of better availability and flexibility, opening the possibility for more thorough, well-controlled investigations to correlate EPs with cancer features.

An animal tumor study in the field utilized combined B_1 magnitude and transceive phase from a quadrature coil at 3T [112]. Both conductivity and permittivity of implanted adenocarcinoma on three rats are reported to be consistent with probe measurements. In another study, Liu et al. successfully demonstrated the conductivity difference between implanted tumor and the surrounding muscle with high sensitivity as shown in Fig. 8d [101]. This study utilized a dedicated 8-channel microstrip transceiver array coil developed for 7T MRI and reconstructed with the gradient-based EPT algorithm [63]. Future studies are expected to take on animal models bearing more resemblance to human cancer and to monitor tumor development along time course.

B. Subject-specific tissue mapping

EPs of normal tissues have been investigated and tabulated using invasive dielectric probes [113], [114]. The Cole-Cole fitting has been performed based on this data, and the resultant curves are widely used in numerical modeling for SAR estimation and thermal dose

computation in hyperthermia [5], [115]. However, organs are intrinsically heterogeneous in composition and structure; their EPs also vary with age [116], [117] and short-term biological effects such as blood supply [118]. Additionally, based on EPT-measured *in vivo* conductivity of muscle in 20 cervical cancer patients, Balidemaj et al. reported a 14% systematic deviation from the Cole-Cole-fitted curve and significant inter-subject variability [107]. These data suggest the necessity of subject-specific EP mapping for precision diagnosis and treatment at personalized level.

C. Other Applications

C.1. In the Brain—A case study of an ischemic stroke patient at 7 T reported that conductivity in the infarction was elevated by a factor of more than two [119]. Another study involves two cases of hemorrhagic and ischemic strokes patients in subacute stage [120], using the recent phase-only EPT reconstruction algorithm that alleviates tissue boundary artifacts [78]. They reported increased conductivity in ischemic lesions and edema, but not hematoma itself, hypothetically due to clot formation.

Taking *a prior* knowledge from quantitative magnetic susceptibility maps for EPT reconstruction, another study investigated conductivity of deep brain nuclei [121]. The reconstructed conductivity and susceptibility are reported to be uncorrelated, suggesting that EPs can provide an additional dimension of information about these important brain structures.

C.2. In the Body—For body imaging, the major challenges fall into the experimental part to obtain reliable B_1 magnitude and phase distributions that are minimally affected by confounding factors, such as B_0 inhomogeneity and motion artifacts. Most previous studies assumed homogeneity of B_1 magnitude in a relatively small ROI and applied phase only conductivity imaging to various organs in the body. SSFP sequence is favorable in these applications due to its insensitivity to B_0 effects and fast speed.

Except for the cervix tumor imaging discussed above, there are three more instances where EPT was utilized to retrieve the conductivity of different body organs, showing the broad spectrum of the potential applications: (1) The livers of 10 healthy subjects were examined using SSFP during inspiration and expiration, leading to conductivity measurements that are consistent with published values [71]. (2) Two isolated perfused pig heart models, one of which with induced severe ischemia, were scanned using gated SSFP, reporting conductivity values of normal tissue close to previous literature and roughly 60% decrease in infarcted area [122]. (3) Five healthy volunteers were recruited for a lung scan, and the expected conductivity difference between inspiration hold and expiration hold was observed [123]. An ultrashort-TE (UTE) sequence was used in this study so as to address the fast signal decay in the lung due to short T2 and severe B_0 inhomogeneity.

C.3. Inferring Electrolyte Concentration—At the Larmor frequency range (>100 MHz), it is expected that the charge-barrier effect of cell membrane on conductivity is weak and conductivity can be directly influenced by ion concentration. Studies in [124] and [125] examined and suggested a linear relationship between sodium concentration measured using sodium MRI and EPT-based conductivity value *in vivo* among different brain tissues. In a

more recent study [126], it was suggested that the portion of free, non-protein-bounded sodium should be accounted for to estimate the conductivity value. Based on these preliminary results, conductivity image measured based on EPT can potentially be used to extract quantitative sodium information while traditional sodium MRI has been hindered by its limited SNR, need of special RF coil and sequence.

Studies also attempted to establish a relationship between water content and EPs in the Larmor frequency range. This effort was done in a study based on protein solution [127] and more recently in *in vivo* MRI measurement [128]. Because increased water content can lead to increased total ion density assuming a constant ion concentration, the unique role of water in defining the conductivity value is not clear. Caution is needed when these models are used to predict conductivity of abnormal tissues which may have an altered ion concentration, e.g. increased sodium in tumor tissue[129].

V. Application of EPT in Prediction of Subject-specific SAR

Local SAR relates to RF-induced local heating of tissue during an MRI scan. Local SAR is required to be determined for any RF coil and RF pulse to be applied to scan the subject. As mentioned earlier, current practice of estimating SAR based on generic human models does not account for the operating status of the RF transmit device or the specific subject's EP distribution. EPT can play an important role in subject-specific SAR estimation because it automatically provides the subject-specific EPs and RF distribution under its framework.

Local SAR is given by

$$\mathrm{SAR} = \frac{\sigma |\mathbf{E}|^2}{2\rho_m} = \frac{\sigma}{2\rho_m} \left| \frac{\nabla \times \mathbf{B}}{\omega \mu_0 \varepsilon_c} \right|^2 \quad (15)$$

where ρ_m is the tissue mass density. Expressing $\mathbf{E}$ via the magnetic field $\mathbf{B}$ using Ampère's Law as done in (15), one can find that determination of local SAR requires not only conductivity, but also permittivity. The determination of conductivity and permittivity is discussed in the previous sections, and are assumed as known quantities in this section. Tissue density is not directly accessible with MR imaging, but is sufficiently constant throughout the body and can be approximated by the density of water around $1\mathrm{g/cm}^3$ (e.g., deviation from muscle and fat tissue is around 5%).

The remaining problem of solving (15) is thus the determination of $\mathbf{B}$. In contrast to the determination of EPs, which can be derived exactly from a single spatial component of $\mathbf{B}$ (assuming constant EPs in (3)), local SAR cannot be derived exactly from a single spatial component of $\mathbf{B}$, even in areas with constant EPs. The MR accessibility of the spatial components B_1^+, B_1^{-*}, which are equivalent to B_x, B_y, as shown in (5), and B_z are summarized in Table I, separately regarding their magnitude and phase. From these six quantities, only the magnitude of B_1^+ is directly measurable via B_1 mapping as discussed above. Three further quantities (magnitude of B_1^{-*} as well as phase of B_1^+ and B_1^{-*}) are influencing the MR signal expressed by (4) but cannot be measured directly. Magnitude and

phase of B_z do not influence the MR signal at all. Different methods about how to estimate the missing quantities are a focus of several studies on EPT-based SAR determination, as discussed in the following.

An additional issue is the scaling of **B**, which cancels out for the calculation of EPs as shown in (8) and (9), and thus, is not required to obtain EPs quantitatively. Such cancellation is not given in (15), and thus, the quantitative determination of local SAR requires the knowledge of the scaling of **B**. Fortunately, this scaling can be obtained in a straightforward manner by comparing measured flip angle, applied RF pulse shape and duration.

Studies on EPT-based local SAR determination are frequently performed with quadrature birdcage coils for head or whole body. Particularly for the central axial plane of such a coil, a couple of assumptions can be applied, which simplify (15) significantly. First, E_z is the dominant component in this plane, and E_x and E_y can be neglected. Calculation of E_z does not depend on the unmeasurable B_z, but only on B_1^+ and B_1^{-*}. Moreover, assuming $\frac{\partial B_z}{\partial z}=0$, $E_z=0$ can be expressed as a function of B_1^+ only [62], [130]

$$|E_z| \approx \frac{2}{|\omega\mu_0\varepsilon_c|}\left|\frac{\partial B_1^+}{\partial x} - i\frac{\partial B_1^+}{\partial y}\right| \quad (16)$$

.

Thus, B_1^+ enables a satisfying estimation of local SAR determination in the central transverse plane of a quadrature volume coil. The determination of B_1^+ can be performed as described in the previous sections for the determination of EPs.

For determination of local SAR of a quadrature volume coil, B_1^{-*} can be treated as zero since $\left|B_1^+\right| >> \left|B_1^{-*}\right|$ when the RF coil is in the transmission mode. This is not the case for imaging, where the coil is switched from RF transmission to RF reception mode yielding $\left|B_1^+\right| \approx \left|B_{1,\text{switched}}^{-*}\right|$, which enables the absolute B_1 phase estimation based on TPA as introduced in Section III.A.

EPT-based local SAR determination has first been studied by phantom experiments using quadrature excitation at 1.5 T, using the assumptions outlined above [52]. The first corresponding *in vivo* results were obtained with the same experimental setup [80], i.e., using quadrature excitation at 1.5T. Shown in Fig. 9a is the local SAR estimation in a middle slice in this study, based on the complex B_1^+ data in Fig. 9a(1) or phase-only data in Fig. 9a(2), in comparison with simulated SAR based on the model of the same setup. Shortly after, the concept was extended to non-quadrature single elements of a transmit coil array at 3T [90], [130] by quantitatively estimating absolute transmit B_1 phase using the MR-measurable multi-channel B_1 data instead of relying on the TPA assumption. In contrast to [90], [130] based on the Helmholtz equation, [62] was based on the full equation (8), deriving absolute transmit and receive phases of each coil element by Gauss's Law and the

extracted proton density at 7 T. The results in this study are illustrated in Fig. 9b, showing consistency between the estimated single-channel local SAR in a healthy subject in reference to the FDTD simulation data. It has been repeatedly shown that after determination of electric fields of the single transmit array elements, the prediction of local SAR for arbitrary B_1-shim settings is possible [130], [131].

Neglecting derivatives of B_z (which is done in all studies mentioned above) is reasonably valid for volume coils as outlined in the previous sections, but less valid for the upcoming type of transmit arrays consisting of local elements ("mattresses"), particularly near transversely oriented parts of conductors. On the other hand, patient-individual SAR determination is of increased interest for these local transmit arrays due to their individual placement on the patient and high-degree-of-freedom RF pulse design. A fast and simple way to estimate B_z for local transmit arrays is possible by integrating B_1^+ and B_1^{-*} via Gauss's Law [132] as

$$B_z(x,y,z) = -\frac{1}{2}\int_{z_0}^{z}\left(\begin{array}{c} \frac{\partial B_1^+(x,y,z')}{\partial x} - i\frac{\partial B_1^+(x,y,z')}{\partial y} \\ +\frac{\partial B_1^{-*}(x,y,z')}{\partial x} + i\frac{\partial B_1^{-*}(x,y,z')}{\partial y} \end{array}\right)dz'. \tag{17}$$

This approach requires that the field of view (FOV) of the measured B_1^+ and B_1^{-*} can be extended in feet-head direction to z_0 with $B_1^+(z_0) \approx B_1^{-*}(z_0) \approx 0$, which is a realistic task for the local surface coils regarded. In contrast, local SAR occurring outside the maximal FOV is a potential drawback investigating transmit body coils.

Once the spatial distribution of the electrical tissue properties is determined, a forward model can be applied to estimate (all spatial components of) the required fields. For EPT-based SAR determination, this has been realized by [133] in the framework of the aforementioned CSI-EPT. However, as mentioned above, a forward model is of considerable effort since it requires not only a model of the subject, but also of the RF coil involved. At least, in contrast to the subject model, the coil model is known *a priori* from the coil's manufacturing. A coil model enables furthermore the determination of the conservative part of the electric field, which is not possible by purely post-processing the measured magnetic field as in (15). Conservative electric fields (obeying Gauss's law and curl-free) are generated predominantly by electronic components of the RF coil, but might be negligible within the body of subject due to their rapid decrease with the distance from the components.

The ultimate goal for RF safety management is the prediction of RF-induced, local tissue temperature increase. In the framework of EPT-based SAR determination, this challenge has been investigated in [131], [134]. It has been shown that prediction of temperature increase is possible, particularly taking heat diffusion into account [134]. Both studies are based on phantoms, justifying the disregard of physiologic temperature regulation, which will become mandatory for corresponding *in vivo* studies. As shown in Fig. 10 from [131], the temperature increase of a specific B_1-shimming mode is predicted by the estimated electric

field of individual transmit elements in the EPT framework and validated with the MR thermometry measurement.

VI. Summary

Electrical properties of biological tissue are related to a broad spectrum of parameters and can be used as biomarkers for diagnosing and monitoring diseases such as tumor, stroke, liver cirrhosis, etc. EPs are also widely used in understanding the interaction of tissue with electromagnetic field for improving the efficacy and accuracy of electromagnetic stimulation or recording in biomedical applications. Much effort has been dedicated to non-invasive and *in vivo* measurement of EPs. Electrical properties tomography has been developed to reconstruct the distribution of EPs based on the MR-measured distribution of B_1 field, which is inherently used in MRI scanners. The high spatial resolution and simple operation on the subject make EPT an interesting and potentially important method for clinical applications related to EPs.

With increasing interest in the field, EPT has gained rapid growth in recent years. Following original demonstration of its feasibility, most effort has been devoted to overcoming the challenges of EPT, including boundary error in the Helmholtz equation-based methods, sensitivity to measurement noise and unmeasurable B_1 component such as its absolute phase and B_z. A fundamental challenge of EPT is that only partial information of the B_1 field can be measured (Table I) so that assumptions are needed for calculation of EPs based on Maxwell's equations. In Section III, we have reviewed major algorithm developments aiming to address these challenges. Among the development, multichannel B_1-based algorithms were proposed for calculating both absolute B_1 phase and EPs with reduced assumptions about the B_1 field, inhomogeneous equations (8) and (9) were used to improve the performance near boundaries, and global solutions were shown promising for addressing both noise sensitivity and boundary issues.

EPT methods have been applied to detect the EP change in diseases such as brain/breast/pelvic tumors, animal tumor models, stroke, etc. Promising results have been reported by comparing with other imaging modalities or validated by probe measurement of EPs. Local solutions using TPA-based phase estimation or phase-only conductivity reconstruction have been the power horse in applications involving patients. This is partially owing to the accessibility of quadrature birdcage RF coils in clinical scanners, available phase data using existing protocols, short scan time and less complicated local Helmholtz-based reconstruction algorithms. Adaptive Laplacian kernel to a reference contrast image with local polynomial fitting was used to avoid boundary errors, at the cost of potential adverse effect from the selected reference image. Future applications should include large-scale studies to demonstrate the value of EPT for a specific subtype of disease in comparison with other existing imaging modalities. For example, EPT can potentially play an important and unique role in detection of tumor in the early stage or differentiation between benign and malignant tumor. At current stage, efforts from multiple research groups on a specific disease model are valuable to demonstrate the clinical impact of EPT methods. Future applications utilizing advanced EPT methods such as multi-channel-based reconstruction or

global solutions are anticipated to achieve high resolution without the potential bias of a reference image.

Fast and subject-specific SAR estimation is an important application of EPT at high field strength. The dynamic SAR estimation can in principle be used to optimize RF pulse design and further MRI development with less conservative RF safety constraints. At higher field, it drives the development of multi-channel EPT methods as the assumptions originally adopted in the early development of EPT are not valid anymore and multi-channel RF transmission becomes common. It is critical to restore the missing field component of B_z for certain RF coils with current running in perpendicular to the B_0 direction. Temperature is the ultimate factor that determines RF safety. Therefore, more accurate heat transfer models need to be developed, considering the estimated SAR, heat transfer rate of different tissues and the convection effect of blood, etc.

Acknowledgments

References

1. Fricke H. The Maxwell-Wagner Dispersion in a Suspension of Ellipsoids. J Phys Chem. Sep; 1953 57(9):934–937.

2. Pethig R. Dielectric Properties of Biological Materials: Biophysical and Medical Applications. IEEE Trans Electr Insul. 1984; EI-19(5):453–474.

3. Hurt WD. Multiterm Debye Dispersion Relations for Permittivity of Muscle. IEEE Trans Biomed Eng. Jan; 1985 BME-32(1):60–64.

4. Foster KR, Schwan HP. Dielectric properties of tissues and biological materials: a critical review. Crit Rev Biomed Eng. 1989; 17(1):25–104. [PubMed: 2651001]

5. Gabriel S, Lau RW, Gabriel C. The dielectric properties of biological tissues: III. Parametric models for the dielectric spectrum of tissues. Phys Med Biol. Nov; 1996 41(11):2271–2293. [PubMed: 8938026]

6. Schwan HP. Electrical properties of tissues and cell suspensions: mechanisms and models. Proceedings of the 16th Annual International Conference of the IEEE Engineering in Medicine and Biology Society, 1994 Engineering Advances: New Opportunities for Biomedical Engineers. 1994; 1:A70–A71.

7. Cole KS, Cole RH. Dispersion and Absorption in Dielectrics I. Alternating Current Characteristics. J Chem Phys. Apr; 1941 9(4):341–351.

8. Surowiec AJ, Stuchly SS, Barr JR, Swarup A. Dielectric properties of breast carcinoma and the surrounding tissues. IEEE Trans Biomed Eng. 1988; 35(4):257–263. [PubMed: 2834285]

9. Joines WT. The measured electrical properties of normal and malignant human tissues from 50 to 900 MHz. Med Phys. 1994; 21(4):547–550. [PubMed: 8058021]

10. Jossinet J. The impedivity of freshly excised human breast tissue. Physiol Meas. Feb; 1998 19(1): 61–75. [PubMed: 9522388]

11. Holder DS. Detection of cerebral ischaemia in the anaesthetised rat by impedance measurement with scalp electrodes: implications for non-invasive imaging of stroke by electrical impedance tomography. Clin Phys Physiol Meas Off J Hosp Phys Assoc Dtsch Ges Für Med Phys Eur Fed Organ Med Phys. Feb; 1992 13(1):63–75.

12. Fallert MA, et al. Myocardial electrical impedance mapping of ischemic sheep hearts and healing aneurysms. Circulation. Jan; 1993 87(1):199–207. [PubMed: 8419008]

13. Lux HD, Heinemann U, Dietzel I. Ionic changes and alterations in the size of the extracellular space during epileptic activity. Adv Neurol. 1986; 44:619–639. [PubMed: 3518349]

14. Assaf BA, Ebersole JS. Continuous Source Imaging of Scalp Ictal Rhythms in Temporal Lobe Epilepsy. Epilepsia. Oct; 1997 38(10):1114–1123. [PubMed: 9579958]

15. He B. Brain electric source imaging: scalp Laplacian mapping and cortical imaging. Crit Rev Biomed Eng. 1999; 27(3–5):149–188. [PubMed: 10864279]

16. Michel CM, Murray MM, Lantz G, Gonzalez S, Spinelli L, Grave de Peralta R. EEG source imaging. Clin Neurophysiol. Oct; 2004 115(10):2195–2222. [PubMed: 15351361]

17. He B, Yang L, Wilke C, Yuan H. Electrophysiological imaging of brain activity and connectivity-challenges and opportunities. IEEE Trans Biomed Eng. Jul; 2011 58(7):1918–1931. [PubMed: 21478071]

18. Yang L, Worrell GA, Nelson C, Brinkmann B, He B. Spectral and spatial shifts of post-ictal slow waves in temporal lobe seizures. Brain J Neurol. Oct; 2012 135(Pt 10):3134–3143.

19. Edelman BJ, Baxter B, He B. EEG Source Imaging Enhances the Decoding of Complex Right-Hand Motor Imagery Tasks. IEEE Trans Biomed Eng. Jan; 2016 63(1):4–14. [PubMed: 26276986]

20. Burnes JE, Taccardi B, MacLeod RS, Rudy Y. Noninvasive ECG Imaging of Electrophysiologically Abnormal Substrates in Infarcted Hearts A Model Study. Circulation. Feb; 2000 101(5):533–540. [PubMed: 10662751]

21. He B, Cohen RJ. Body surface Laplacian mapping of cardiac electrical activity. Am J Cardiol. Dec; 1992 70(20):1617–1620. [PubMed: 1466337]

22. Liu Z, Liu C, He B. Noninvasive reconstruction of three-dimensional ventricular activation sequence from the inverse solution of distributed equivalent current density. IEEE Trans Med Imaging. Oct; 2006 25(10):1307–1318. [PubMed: 17024834]

23. Zhou Z, Jin Q, Chen LY, Yu L, Wu L, He B. Noninvasive Imaging of High-Frequency Drivers and Reconstruction of Global Dominant Frequency Maps in Patients With Paroxysmal and Persistent Atrial Fibrillation. IEEE Trans Biomed Eng. Jun; 2016 63(6):1333–1340. [PubMed: 27093312]

24. Potyagaylo D, Dossel O, van Dam P. Influence of Modeling Errors on the Initial Estimate for Nonlinear Myocardial Activation Times Imaging Calculated With Fastest Route Algorithm. IEEE Trans Biomed Eng. Dec; 2016 63(12):2576–2584. [PubMed: 27164568]

25. Benabid AL, et al. Long-term suppression of tremor by chronic stimulation of the ventral intermediate thalamic nucleus. Lancet Lond Engl. Feb; 1991 337(8738):403–406.

26. Limousin P, et al. Electrical Stimulation of the Subthalamic Nucleus in Advanced Parkinson's Disease. N Engl J Med. Oct; 1998 339(16):1105–1111. [PubMed: 9770557]

27. Johnson MD, et al. Neuromodulation for Brain Disorders: Challenges and Opportunities. IEEE Trans Biomed Eng. Mar; 2013 60(3):610–624. [PubMed: 23380851]

28. Roy A, Baxter B, He B. High-definition transcranial direct current stimulation induces both acute and persistent changes in broadband cortical synchronization: a simultaneous tDCS-EEG study. IEEE Trans Biomed Eng. Jul; 2014 61(7):1967–1978. [PubMed: 24956615]

29. George M, Lisanby S, Sackeim H. Transcranial magnetic stimulation: Applications in neuropsychiatry. Arch Gen Psychiatry. Apr; 1999 56(4):300–311. [PubMed: 10197824]

30. Pappone C, et al. Circumferential Radiofrequency Ablation of Pulmonary Vein Ostia A New Anatomic Approach for Curing Atrial Fibrillation. Circulation. Nov; 2000 102(21):2619–2628. [PubMed: 11085966]

31. Hiraoka M, et al. Clinical results of radiofrequency hyperthermia combined with radiation in the treatment of radioresistant cancers. Cancer. Dec; 1984 54(12):2898–2904. [PubMed: 6498766]

32. Barber CC, Brown BH. Imaging spatial distributions of resistivity using applied potential tomography. Electron Lett. Oct; 1983 19(22):933–935.

33. Paulson K, Lionheart W, Pidcock M. Optimal experiments in electrical impedance tomography. IEEE Trans Med Imaging. Dec; 1993 12(4):681–686. [PubMed: 18218462]

34. Metherall P, Barber DC, Smallwood RH, Brown BH. Three-dimensional electrical impedance tomography. Nature. 1996; 380(6574):509–512. [PubMed: 8606768]

35. Mueller JL, Isaacson D, Newell JC. A reconstruction algorithm for electrical impedance tomography data collected on rectangular electrode arrays. IEEE Trans Biomed Eng. Nov; 1999 46(11):1379–1386. [PubMed: 10582423]

36. Brown B. Electrical impedance tomography (EIT): a review. J Med Eng Technol. May; 2003 27(3): 97–108. [PubMed: 12775455]

37. Oh SH, Han JY, Lee SY, Cho MH, Lee BI, Woo EJ. Electrical conductivity imaging by magnetic resonance electrical impedance tomography (MREIT). Magn Reson Med. Oct; 2003 50(4):875– 878. [PubMed: 14523975]

38. Seo JK, Yoon J-R, Woo EJ, Kwon O. Reconstruction of conductivity and current density images using only one component of magnetic field measurements. IEEE Trans Biomed Eng. 2003; 50(9): 1121–1124. [PubMed: 12943280]

39. Park C, Park E-J, Woo EJ, Kwon O, Seo JK. Static conductivity imaging using variational gradient Bz algorithm in magnetic resonance electrical impedance tomography. Physiol Meas. Feb; 2004 25(1):257–269. [PubMed: 15005320]

40. Gao N, Zhu SA, He B. Estimation of electrical conductivity distribution within the human head from magnetic flux density measurement. Phys Med Biol. Jun; 2005 50(11):2675–2687. [PubMed: 15901962]

41. Gao N, Zhu SA, He B. A new magnetic resonance electrical impedance tomography (MREIT) algorithm: the RSM-MREIT algorithm with applications to estimation of human head conductivity. Phys Med Biol. Jun.2006 51(12):3067. [PubMed: 16757863]

42. Kim HJ, et al. Conductivity imaging of canine brain using a 3 T MREIT system: postmortem experiments. Physiol Meas. 2007; 28(11):1341–1353. [PubMed: 17978419]

43. Seo JK, et al. Local Harmonic Algorithm With Domain Decomposition in MREIT: Computer Simulation Study. IEEE Trans Med Imaging. Dec; 2008 27(12):1754–1761. [PubMed: 19033091]

44. Woo EJ, Seo JK. Magnetic resonance electrical impedance tomography (MREIT) for high-resolution conductivity imaging. Physiol Meas. Oct; 2008 29(10):R1–26. [PubMed: 18799834]

45. Kim HJ, et al. In Vivo High-ResolutionConductivity Imaging of the Human Leg Using MREIT: The First Human Experiment. Med Imaging IEEE Trans On. 2009; 28(11):1681–1687.

46. Xu Y, He B. Magnetoacoustic tomography with magnetic induction (MAT-MI). Phys Med Biol. Nov; 2005 50(21):5175–5187. [PubMed: 16237248]

47. Li X, Xu Y, He B. Imaging Electrical Impedance From Acoustic Measurements by Means of Magnetoacoustic Tomography With Magnetic Induction (MAT-MI). IEEE Trans Biomed Eng. Feb; 2007 54(2):323–330. [PubMed: 17278589]

48. Hu G, Cressman E, He B. Magnetoacoustic imaging of human liver tumor with magnetic induction. Appl Phys Lett. Jan.2011 98(2):23703. [PubMed: 21301635]

49. Mariappan L, He B. Magnetoacoustic Tomography with Magnetic Induction: Bioimepedance reconstruction through vector source imaging. IEEE Trans Med Imaging. Jan; 2013 32(3):619–627. [PubMed: 23322761]

50. Haacke EM, Petropoulos LS, Nilges EW, Wu DH. Extraction of conductivity and permittivity using magnetic resonance imaging. Phys Med Biol. Jun; 1991 36(6):723–734.

51. Wen, H. Proc SPIE. Vol. 5030. San Diego, CA, USA: 2003. Noninvasive quantitative mapping of conductivity and dielectric distributions using RF wave propagation effects in high-field MRI; p. 471-477.

52. Katscher U, Voigt T, Findeklee C, Vernickel P, Nehrke K, Dossel O. Determination of Electric Conductivity and Local SAR Via B1 Mapping. Med Imaging IEEE Trans On. Sep; 2009 28(9): 1365–1374.

53. Zhang X, Zhu S, He B. Imaging Electric Properties of Biological Tissues by RF Field Mapping in MRI. IEEE Trans Med Imaging. Feb; 2010 29(2):474–481. [PubMed: 20129847]

54. Katscher U, Börnert P, Leussler C, van den Brink JS. Transmit SENSE. Magn Reson Med. Jan; 2003 49(1):144–150. [PubMed: 12509830]

55. Zhu Y. Parallel excitation with an array of transmit coils. Magn Reson Med. Apr; 2004 51(4):775–784. [PubMed: 15065251]

56. Maxwell JC. A Dynamical Theory of the Electromagnetic Field. Philos Trans R Soc Lond. Jan. 1865 155:459–512.

57. Fleisch, D. A Student's Guide to Maxwell's Equations. Cambridge University Press; 2008.

58. Hoult DI. The principle of reciprocity in signal strength calculations—A mathematical guide. Concepts Magn Reson. Jan; 2000 12(4):173–187.

59. Insko EK, Bolinger L. Mapping of the Radiofrequency Field. J Magn Reson A. Jun; 1993 103(1): 82–85.

60. Yarnykh VL. Actual flip angle imaging in the pulsed steady state: A method for rapid three dimensional mapping of the transmitted radiofrequency field. Magn Reson Med. Jan; 2007 57(1): 192–200. [PubMed: 17191242]

61. Nehrke K, Börnert P. DREAM—a novel approach for robust, ultrafast, multislice B1 mapping. Magn Reson Med. 2012; 68(5):1517–1526. [PubMed: 22252850]

62. Zhang X, Schmitter S, Van de Moortele P-F, Liu J, He B. From Complex B1 Mapping to Local SAR Estimation for Human Brain MR Imaging Using Multi-channel Transceiver Coil at 7T. IEEE Trans Med Imaging. Mar; 2013 32(6):1058–1067. [PubMed: 23508259]

63. Liu J, Zhang X, Schmitter S, Van de Moortele P-F, He B. Gradient-based electrical properties tomography (gEPT): A robust method for mapping electrical properties of biological tissues in vivo using magnetic resonance imaging. Magn Reson Med. Sep; 2015 74(3):634–646. [PubMed: 25213371]

64. Sacolick LI, Wiesinger F, Hancu I, Vogel MW. B1 mapping by Bloch-Siegert shift. Magn Reson Med. 2010; 63(5):1315–1322. [PubMed: 20432302]

65. Duan Q, van Gelderen P, Duyn J. Improved Bloch-Siegert based B1 mapping by reducing off-resonance shift. NMR Biomed. Sep; 2013 26(9):1070–1078. [PubMed: 23355474]

66. Hayes CE, Edelstein WA, Schenck JF, Mueller OM, Eash M. An efficient, highly homogeneous radiofrequency coil for whole-body NMR imaging at 1.5 T. J Magn Reson 1969. Jul; 1985 63(3): 622–628.

67. Voigt T, Katscher U, Doessel O. Quantitative conductivity and permittivity imaging of the human brain using electric properties tomography. Magn Reson Med. 2011; 66(2):456–466. [PubMed: 21773985]

68. van Lier AL, et al. B 1+ Phase mapping at 7 T and its application for in vivo electrical conductivity mapping. Magn Reson Med. 2012; 67(2):552–561. [PubMed: 21710613]

69. Lee S-K, Bulumulla S, Wiesinger F, Sacolick L, Sun W, Hancu I. Tissue electrical property mapping from zero echo-time magnetic resonance imaging. IEEE Trans Med Imaging. Feb; 2015 34(2):541–550. [PubMed: 25312919]

70. Stehning, C., Voigt, T., Katscher, U. Real-Time Conductivity Mapping using Balanced SSFP and Phase-Based Reconstruction; Proceedings of the 19th Annual Meeting of ISMRM; Montreal, Canada. 2011. p. 128

71. Stehning, C., Voigt, T., Karkowski, P., Katscher, U., Philips Research. Electric Properties Tomography (EPT) of the Liver in a Single Breathhold Using SSFP; Proceedings of the 20th Annual Meeting of ISMRM; Melbourne, Australia. 2012. p. 386

72. Seo JK, et al. Error analysis of nonconstant admittivity for MR-based electric property imaging. IEEE Trans Med Imaging. Feb; 2012 31(2):430–437. [PubMed: 21990329]

73. Duan S, Xu C, Deng G, Wang J, Liu F, Xin SX. Quantitative analysis of the reconstruction errors of the currently popular algorithm of magnetic resonance electrical property tomography at the interfaces of adjacent tissues. NMR Biomed. Jun; 2016 29(6):744–750. [PubMed: 27037715]

74. Katscher, U., et al. Estimation of Breast Tumor Conductivity using Parabolic Phase Fitting; presented at the ISMRM; Melbourne, Australia. 2012. p. 3482

75. Lee J, Shin J, Kim D-H. MR-based conductivity imaging using multiple receiver coils. Magn Reson Med. Aug; 2016 76(2):530–539. [PubMed: 26375762]

76. Liu J, Van de Moortele P-F, Zhang X, Wang Y, He B. Simultaneous Quantitative Imaging of Electrical Properties and Proton Density from B1 Maps Using MRI. IEEE Trans Med Imaging. 2016; 35(9):2064–2073. [PubMed: 28005010]

77. Hafalir FS, Oran OF, Gurler N, Ider YZ. Convection-reaction equation based magnetic resonance electrical properties tomography (cr-MREPT). IEEE Trans Med Imaging. Mar; 2014 33(3):777–793. [PubMed: 24595349]

78. Gurler N, Ider YZ. Gradient-based electrical conductivity imaging using MR phase. Magn Reson Med. Jan; 2017 77(1):137–150. [PubMed: 26762771]

79. Hurt WD, Ziriax JM, Mason PA. Variability in EMF permittivity values: implications for SAR calculations. IEEE Trans Biomed Eng. Mar; 2000 47(3):396–401. [PubMed: 10743782]

80. Voigt T, Homann H, Katscher U, Doessel O. Patient-individual local SAR determination: in vivo measurements and numerical validation. Magn Reson Med. Oct; 2012 68(4):1117–1126. [PubMed: 22213053]

81. Roemer PB, Edelstein WA, Hayes CE, Souza SP, Mueller OM. The NMR phased array. Magn Reson Med. Nov; 1990 16(2):192–225. [PubMed: 2266841]

82. Ledden PJ, de Zwart JA, Bodurka J, van Gelderen P, Chu R, Duyn JH. Signal-to-noise ratio and parallel imaging performance of a 16-channel receive-only brain coil array at 3.0 Tesla. Magn Reson Med. Jan; 2004 51(1):22–26. [PubMed: 14705041]

83. Sodickson DK, Manning WJ. Simultaneous acquisition of spatial harmonics (SMASH): Fast imaging with radiofrequency coil arrays. Magn Reson Med. Oct; 1997 38(4):591–603. [PubMed: 9324327]

84. Pruessmann KP, Weiger M, Scheidegger MB, Boesiger P. SENSE: sensitivity encoding for fast MRI. Magn Reson Med. Nov; 1999 42(5):952–962. [PubMed: 10542355]

85. Griswold MA, et al. Generalized autocalibrating partially parallel acquisitions (GRAPPA). Magn Reson Med. Jun; 2002 47(6):1202–1210. [PubMed: 12111967]

86. Lee S-K, Bulumulla S, Hancu I. Theoretical Investigation of Random Noise-Limited Signal-to-Noise Ratio in MR-Based Electrical Properties Tomography. IEEE Trans Med Imaging. Nov; 2015 34(11):2220–2232. [PubMed: 25955582]

87. Zhang X, Van de Moortele P-F, Schmitter S, He B. Complex B1 mapping and electrical properties imaging of the human brain using a 16-channel transceiver coil at 7T. Magn Reson Med. May; 2013 69(5):1285–1296. [PubMed: 22692921]

88. Liu J, Zhang X, Van de Moortele P-F, Schmitter S, He B. Determining electrical properties based on B(1) fields measured in an MR scanner using a multi-channel transmit/receive coil: a general approach. Phys Med Biol. Jul; 2013 58(13):4395–4408. [PubMed: 23743673]

89. Marques JP, Sodickson DK, Ipek O, Collins CM, Gruetter R. Single acquisition electrical property mapping based on relative coil sensitivities: A proof-of-concept demonstration. Magn Reson Med. Jul; 2015 74(1):185–195.

90. Katscher U, Findeklee C, Voigt T. B1-based specific energy absorption rate determination for nonquadrature radiofrequency excitation. Magn Reson Med. 2012; 68(6):1911–1918. [PubMed: 22374804]

91. Sodickson, D., et al. Local Maxwell Tomography Using Transmit-Receive Coil Arrays for Contact-Free Mapping of Tissue Electrical Properties and Determination of Absolute RF Phase; Proceedings of the 20th Annual Meeting of ISMRM; Melbourne, Australia. 2012. p. 388

92. Sodickson, D., et al. Generalized Local Maxwell Tomography for Mapping of Electrical Property Gradients and Tensors; Proceedings of the 21th Annual Meeting of ISMRM; Salt Lake City, USA. 2013. p. 4175

93. Iserles, A. A first course in the numerical analysis of differential equations. 2nd. Cambridge, UK ; New York: Cambridge University Press; 2009.

94. Balidemaj E, et al. CSI-EPT: A Contrast Source Inversion Approach for Improved MRI-Based Electric Properties Tomography. IEEE Trans Med Imaging. Sep; 2015 34(9):1788–1796. [PubMed: 25706578]

95. Schmidt R, Webb A. A new approach for electrical properties estimation using a global integral equation and improvements using high permittivity materials. J Magn Reson. Jan.2016 262:8–14. [PubMed: 26679289]

96. Serralles, J., et al. presented at the Proc Intl Soc Mag Reson Med. Vol. 24. Singapore: 2016. Global Maxwell Tomography: a novel technique for electrical properties mapping without symmetry assumptions or edge artifacts; p. 2993

97. Ammari H, Kwon H, Lee Y, Kang K, Seo JK. Magnetic resonance-based reconstruction method of conductivity and permittivity distributions at the Larmor frequency. Inverse Probl. 2015; 31(10): 105001.

98. Wang, Y., Van de Moortele, P-F., He, B. CONtrast Conformed Electrical Properties Tomography (CONCEPT) based on Multi-channel Transmission; Proceedings of the 25th Annual Meeting of ISMRM; Honolulu, HI, USA. 2017. p. 3640

99. Borsic A, Perreard I, Mahara A, Halter RJ. An Inverse Problems Approach to MR-EPT Image Reconstruction. IEEE Trans Med Imaging. Jan; 2016 35(1):244–256. [PubMed: 26302510]

100. Ropella KM, Noll DC. A regularized, model-based approach to phase-based conductivity mapping using MRI. Magn Reson Med. Dec.2016

101. Liu J, et al. In vivo imaging of electrical properties of an animal tumor model with an 8-channel transceiver array at 7 T using electrical properties tomography. Magn Reson Med. Jan.2017

102. Ider, YZ., Ariturk, G., Yildiz, G. Spatial and Contrast Resolution of Phase Based MREPT; Proceedings of the 25th Annual Meeting of ISMRM; Honolulu, HI, USA. 2017. p. 3642

103. Katscher, U., Abe, H., Ivancevic, M., Djamshidi, K., Karkowski, P., Newstead, G. Towards the investigation of breast tumor malignancy via electric conductivity measurement; Proceedings of the 21th Annual Meeting of ISMRM; Salt Lake City, USA. 2013. p. 3372

104. Shin J, et al. Initial study on in vivo conductivity mapping of breast cancer using MRI. J Magn Reson Imaging JMRI. 2015; 42(2):371–378. [PubMed: 25413153]

105. Kim S-Y, et al. Correlation between conductivity and prognostic factors in invasive breast cancer using magnetic resonance electric properties tomography (MREPT). Eur Radiol. Jul; 2016 26(7): 2317–2326. [PubMed: 26497503]

106. Balidemaj E, Crezee H, van Lier ALHMW, Nederveen AJ, Stalpers LJA, van den Berg CAT. Feasibility of Electric Property Tomography of pelvic tumors at 3T. Magn Reson Med. Apr; 2015 73(4):1505–1513. [PubMed: 24777618]

107. Balidemaj E, et al. In vivo electric conductivity of cervical cancer patients based on B1+ maps at 3T MRI. Phys Med Biol. 2016; 61(4):1596. [PubMed: 26836010]

108. van Lier, AL., et al. Electrical conductivity imaging of brain tumours; Proceedings of the 19th Annual Meeting of ISMRM; Montreal, Canada. 2011. p. 4464

109. Voigt, T., Vaterlein, O., Stehning, C., Katscher, U., Fiehler, J. In vivo Glioma Characterization using MR Conductivity Imaging; Proceedings of the 19th Annual Meeting of ISMRM; Montreal, QC, Canada. 2011. p. 127

110. Tha, KK., et al. Noninvasive Evaluation of Electrical Conductivity of the Normal Brain and Brain Tumors; Proceedings of the 22nd Annual Meeting of ISMRM; Milan, Italy. 2014. p. 1885

111. Tha, KK., et al. Electrical Conductivity Characteristics of Meningiomas: Noninvasive Assessment using Electric Properties Tomography; Proceedings of the 23rd Annual Meeting of ISMRM; Toronto, ON, Canada. 2015. p. 4397

112. Bulumulla, S., Roberts, J., Lee, S-K., Lamb, P., Hancu, I. Reference aided imaging of rat tumor dielectric properties at 3.0T. Milan, Italy: 2014. p. 3193

113. Gabriel C, Gabriel S, Corthout E. The dielectric properties of biological tissues: I. Literature survey. Phys Med Biol. Nov.1996 41:2231–2249. [PubMed: 8938024]

114. Gabriel S, Lau RW, Gabriel C. The dielectric properties of biological tissues: II. Measurements in the frequency range 10 Hz to 20 GHz. Phys Med Biol. Nov; 1996 41(11):2251–2269. [PubMed: 8938025]

115. Christ A, et al. The Virtual Family–development of surface-based anatomical models of two adults and two children for dosimetric simulations. Phys Med Biol. Jan; 2010 55(2):N23–38. [PubMed: 20019402]

116. Peyman A, Rezazadeh AA, Gabriel C. Changes in the dielectric properties of rat tissue as a function of age at microwave frequencies. Phys Med Biol. Jun.2001 46(6):1617. [PubMed: 11419623]

117. Peyman A, Holden SJ, Watts S, Perrott R, Gabriel C. Dielectric properties of porcine cerebrospinal tissues at microwave frequencies: in vivo, in vitro and systematic variation with age. Phys Med Biol. 2007; 52(8):2229. [PubMed: 17404466]

118. Semenov S, Huynh T, Williams T, Nicholson B, Vasilenko A. Dielectric properties of brain tissue at 1 GHz in acute ischemic stroke: Experimental study on swine. Bioelectromagnetics. Feb; 2017 38(2):158–163. [PubMed: 27901288]

119. van Lier, ALHMW., et al. Electrical conductivity in ischemic stroke at 7.0 Tesla: A Case Study; Proceedings of the 20th Annual Meeting of ISMRM; Melbourne, Australia. 2012. p. 3484

120. Gurler, N., Oran, OF., Keklikoglu, HD., Ider, YZ. Application of Generalized Phase based Electrical Conductivity Imaging in the Subacute Stage of Hemorrhagic and Ischemic Strokes; Proceedings of the 25th Annual Meeting of ISMRM; Singapore. 2016. p. 2994

121. Katscher, U., Gagiyev, M., Meineke, J. Conductivity Determination of Deep Gray Matter Nuclei Utilizing Susceptibility-Based Delineation; Proceedings of the 25th Annual Meeting of ISMRM; Singapore. 2016. p. 3336

122. Voigt, T., et al. Conductivity Imaging of an Ischemic Pig Heart Model Using Electric Properties Tomography; Proceedings of the 20th Annual Meeting of ISMRM; Melbourne, Australia. 2012. p. 3483

123. Katscher, U., Bornert, P. Imaging of Lung Conductivity Using Ultrashort Echo-Time Imaging; Proceedings of the 25th Annual Meeting of ISMRM; Singapore. 2016. p. 2923

124. van Lier, ALHMW., et al. 23Na-MRI and EPT: Are sodium concentration and electrical conductivity at 298 MHz (7T) related?; Proceedings of the 21th Annual Meeting of ISMRM; Salt Lake City, USA. 2013. p. 115

125. Liao, Y., Romanzetti, S., Gras, V., Huang, D., Shah, NJ. The dielectric properties of brain tissues: variation in electrical conductivity with tissue sodium concentration and tissue water content at 3T/4T; Proceedings of the 23th Annual Meeting of ISMRM; Toronto, ON, Canada. 2015. p. 3302

126. Mandija, S., Webb, A., de Bruin, P., Luijten, P., van den Berg, CAT. Investigating the relation between electrical conduction and tissue composition with proton and sodium MRI; Proceedings of the 25th Annual Meeting of ISMRM; Honolulu, HI, USA. 2017. p. 3639

127. Bull HB, Breese K. Electrical conductance of protein solutions. J Colloid Interface Sci. Mar; 1969 29(3):492–495. [PubMed: 5790356]

128. Michel E, Hernandez D, Lee SY. Electrical conductivity and permittivity maps of brain tissues derived from water content based on T1-weighted acquisition. Magn Reson Med. Mar.2016 n/a-n/a.

129. Ouwerkerk R, Bleich KB, Gillen JS, Pomper MG, Bottomley PA. Tissue Sodium Concentration in Human Brain Tumors as Measured with 23Na MR Imaging. Radiology. May; 2003 227(2):529–537. [PubMed: 12663825]

130. Buchenau S, Haas M, Splitthoff DN, Hennig J, Zaitsev M. Iterative separation of transmit and receive phase contributions and B_1+-based estimation of the specific absorption rate for transmit arrays. Magn Reson Mater Phys Biol Med. Sep.2013 :1–14.

131. Zhang X, Liu J, de Moortele P-FV, Schmitter S, He B. Quantitative prediction of radio frequency induced local heating derived from measured magnetic field maps in magnetic resonance imaging: A phantom validation at 7 T. Appl Phys Lett. Dec.2014 105(24):244101. [PubMed: 25565707]

132. Katscher, U., et al. B1-based SAR determination for local RF transmit coils; Proceedings of the 23rd Annual Meeting of ISMRM; Toronto, ON, Canada. 2015. p. 383

133. Balidemaj E, et al. B1-based SAR reconstruction using contrast source inversion-electric properties tomography (CSI-EPT). Med Biol Eng Comput. Feb; 2017 55(2):225–233. [PubMed: 27108291]

134. Boulant, N., Katscher, U., Luong, M., Massire, A., Amadon, A., Vignaud, A. B1+-based SAR assessment using a birdcage coil at 7 Tesla: experimental evaluation using magnetic resonance thermometry; Proceedings of the 23th Annual Meeting of ISMRM; Milan, Italy. 2014. p. 4900
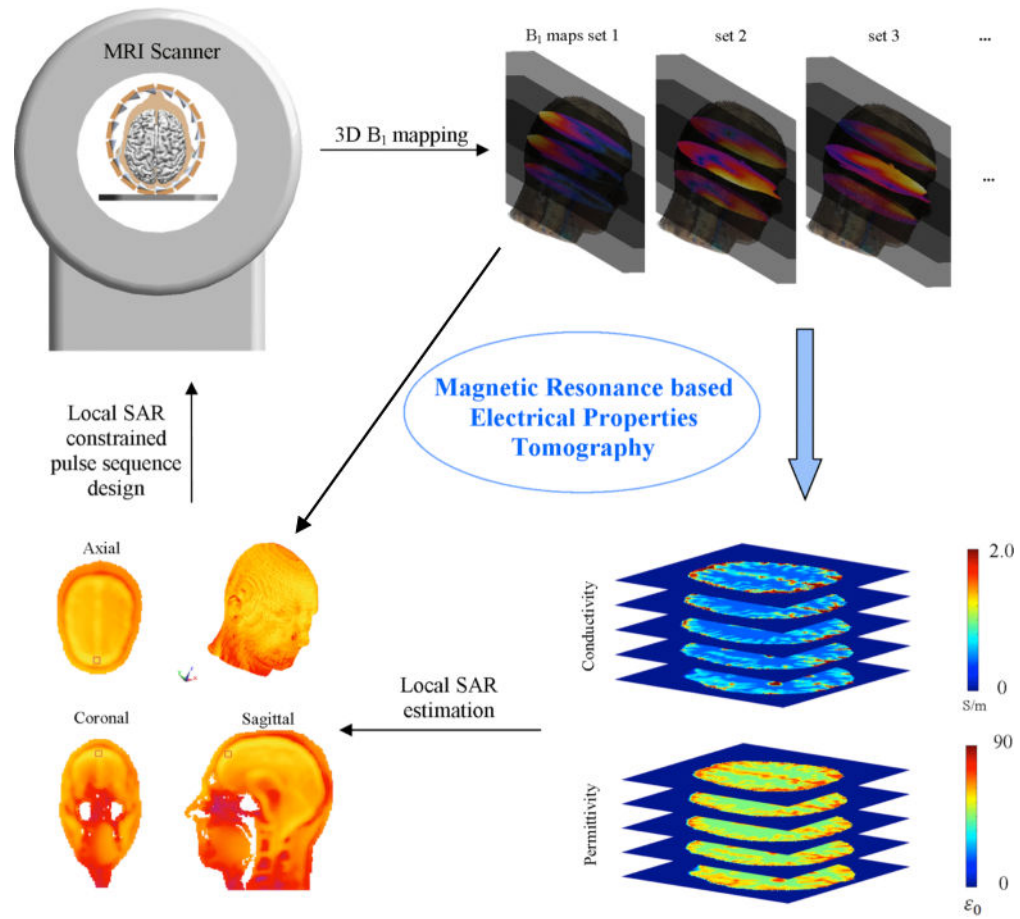
Fig. 1.
Schematic diagram illustrating electrical properties tomography and its application in imaging tissue electrical properties and predicting subject-specific absorption rate.
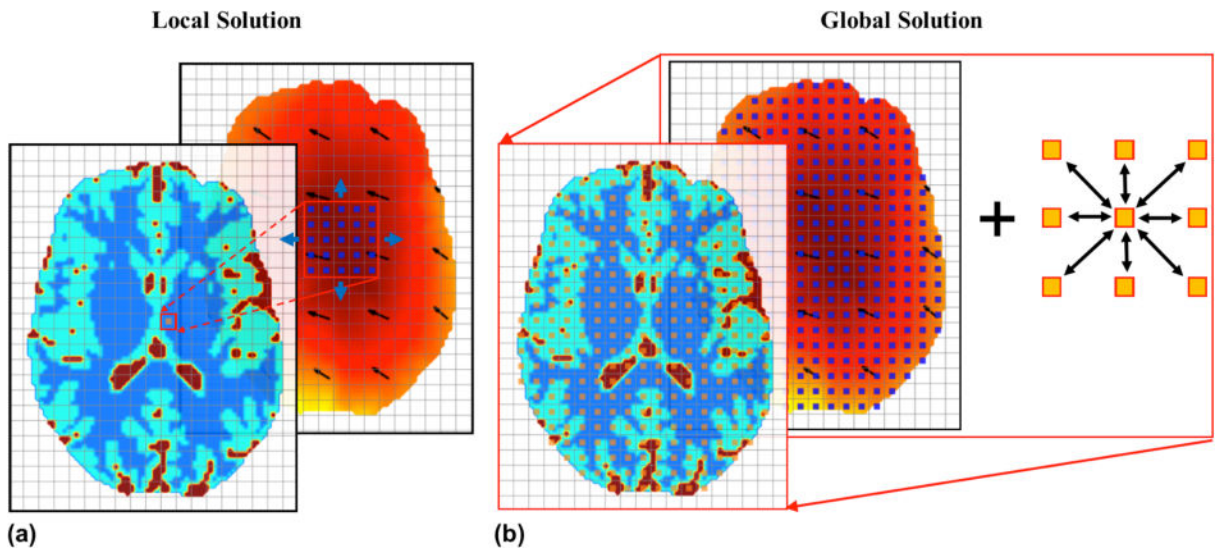
Fig. 2.
Illustration of local EPT reconstruction solutions in comparison with global EPT solutions. Using a local solution (a), EPs on each voxel are determined solely by the measured B_1 data within its small neighborhood. On the other hand, a global solution (b) is obtained using all the voxels containing measurement information and by exploiting the inter-voxel relationship of EPs (indicated by arrows) to constrain the solution.
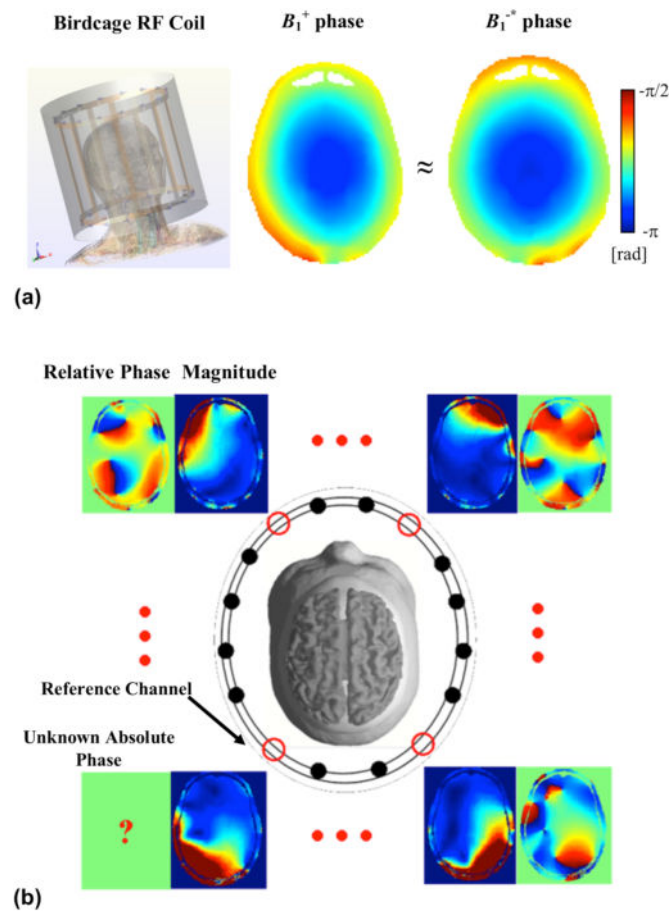
Fig. 3.
(a) Left: simulation model of a quadrature birdcage RF coil loaded with a realistic human head model at 3T; right: the simulated phase distributions of the transmit and receive B_1 fields are approximately equal. (b) Diagram showing measurable B_1 data, including magnitude and relative phase using a multi-channel transmit or receive RF coil array; the data shown is measured $|B_1^+|$ and corresponding relative phase in a human subject at 7 T.
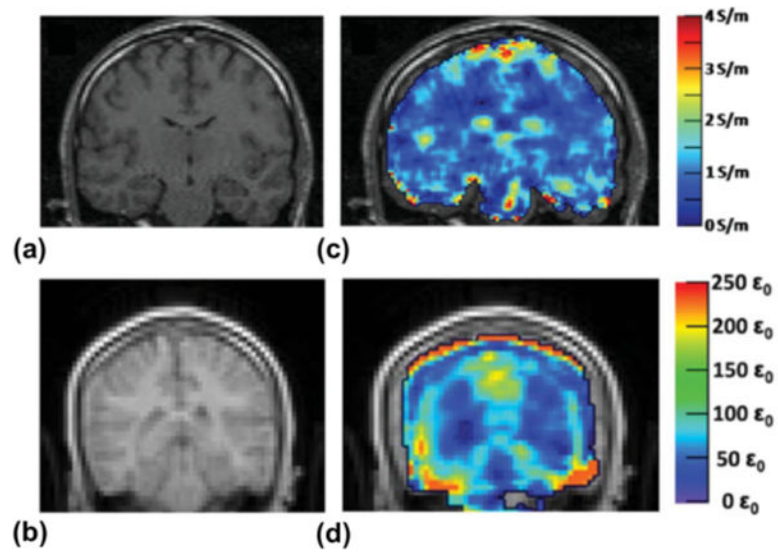
Fig. 4.
Results of reconstructed EPs of healthy human brain tissue *in vivo*. (a) and (b) Magnitude of MRI data for reconstruction of EPs in (c) conductivity and (d) permittivity, respectively. EPs were reconstructed using equation (10), magnitude B_1^+ and estimated phase based on TPA. Reproduced with permission from Voigt, Katscher and Doessel. Magn Reson Med 2011; 66:456–466.
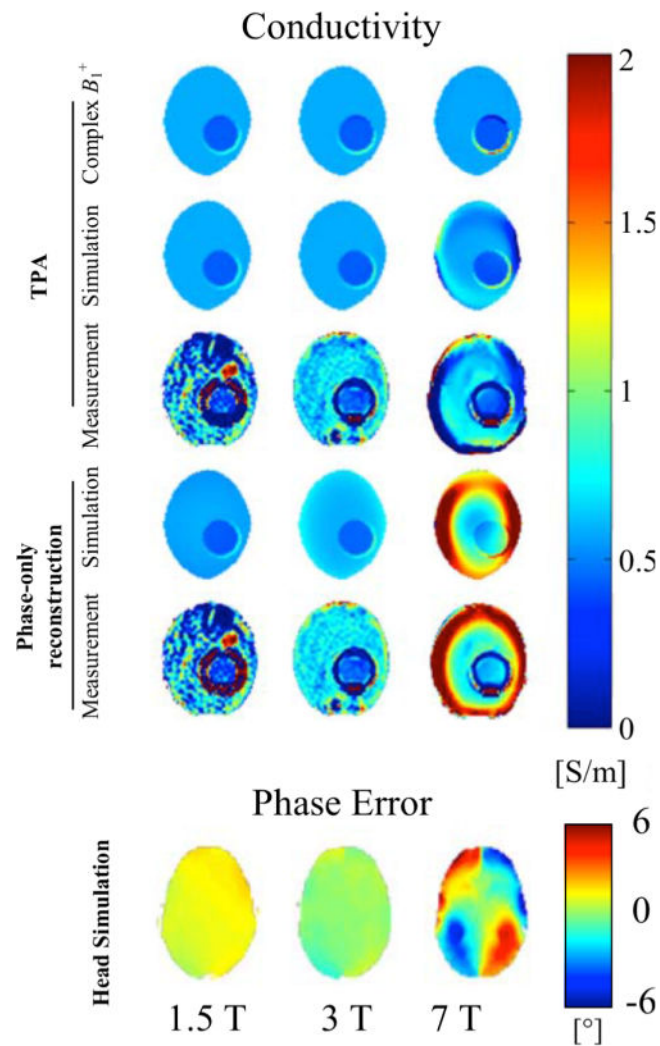
Fig. 5.
Top: TPA-based and phase-only conductivity reconstruction using measured and simulated B_1^+ data of a phantom (model) at different field strengths, respectively. Bottom: Error of TPA phase estimation based on simulated B_1^+ with a realistic head model at different field strengths. Reproduced with permission from van Lier et al. Magn Reson Med 2013; 71:354–363.
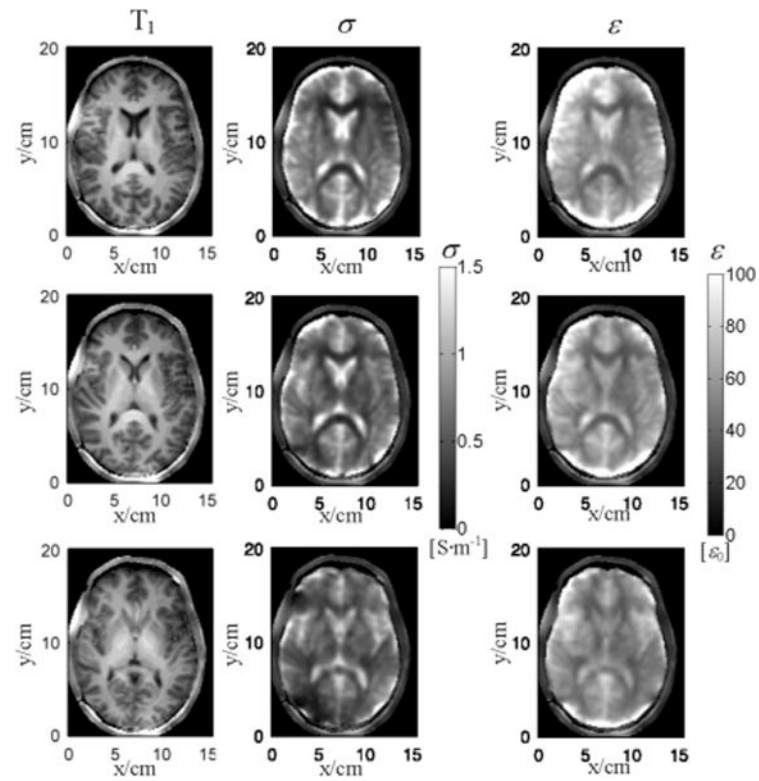
Fig. 6.
Reconstructed *in vivo* EPs using the gradient-based EPT algorithm in three slices of a healthy human subject's brain. Left: reference T1-weighted images; middle: reconstructed conductivity images; right: reconstructed permittivity images. Reproduced with permission from Liu et al., 2015; 74: 634–646.
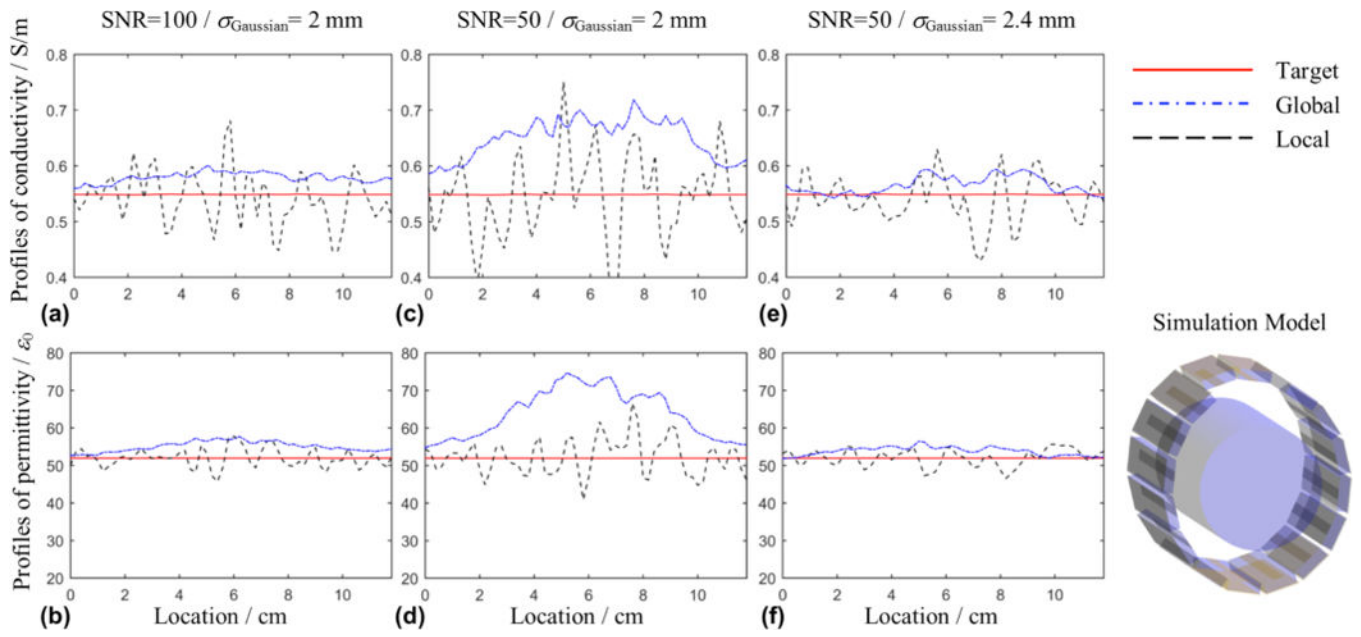
Fig. 7.
A comparison of noise effect on EPT reconstruction between a global and local solution based on a finite-difference time-domain simulation using a 16-channel microstrip RF array coil [92] loaded with a cylindrical homogeneous phantom model (σ: 0.55 S/m and ε: 52 ε_0) at 7 T.
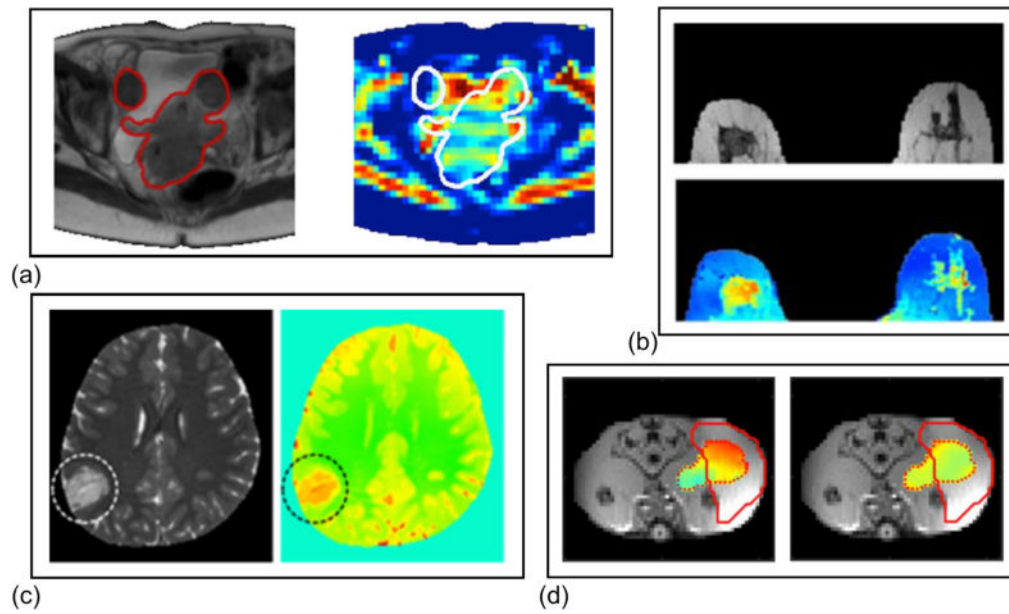
Fig. 8.
(a) Cervix tumor delineated on anatomical image and projected onto conductivity map. Reproduced with permission from Balidemaj et al., Magn Reson Med 2015; 73:1505–1513. (b) Anatomical and conductivity images of the breast of a tubular carcinoma patient. Reproduced with permission from Shin et al., J Magn Reson Imaging 2015; 42:371–378. (c) Dysembryoplastic neuroepithelial tumor showing hyper-intensity on SSFP and its conductivity distribution [110]. (d) Conductivity and permittivity overlaid on proton density-weighted image of a rat tumor xenograft model. Reproduced with permission from Liu et al., Magn Reson Med 2017.
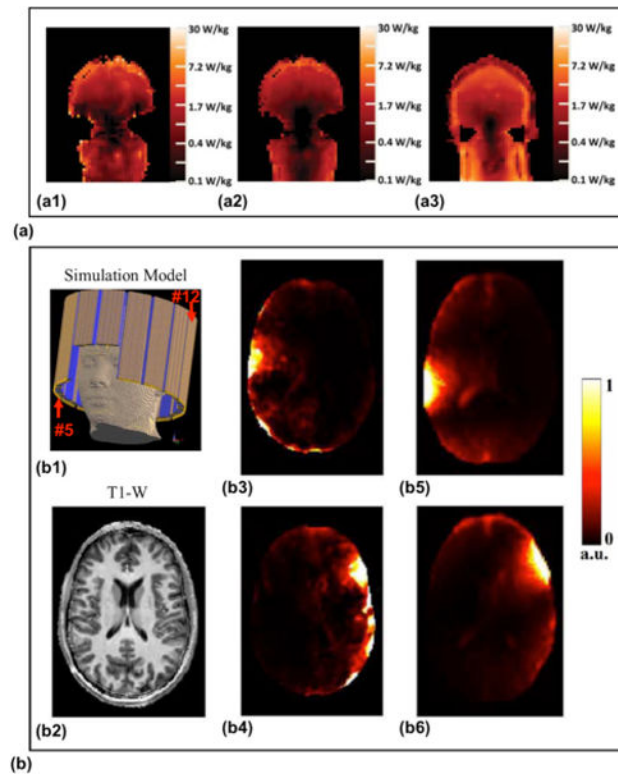
Fig. 9.
EPT-based local SAR estimation under *in vivo* setups. (a) Local SAR distribution with a quadrature birdcage RF coil at 1.5 T: (a1) local SAR estimation based on measured complex B_1^+ data; (a2) local SAR estimation using the phase-only method; (a3) simulated SAR distribution. (b) Local SAR distribution of individual channels with a 16-channel microstrip transceive RF array coil at 7 T: (b1) the simulation model showing the RF coil; (b2) a T1-weighted image of the imaged slice; (b3) and (b4) local SAR estimation of channel #5 and #12, respectively; (b5) and (b6) simulated local SAR of the two channels. (a) was reproduced with permission from Voigt et al., Magn Reson Med 2012; 68:1117–1126, and (b) was reproduced permission from Zhang et al., IEEE Trans Med Imaging 2013; 32:1058–1067
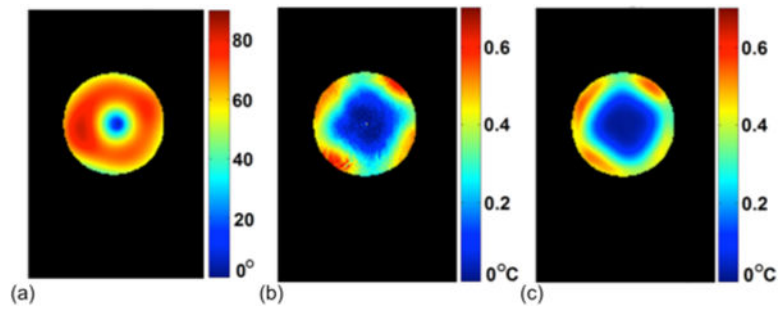
Fig. 10.
Prediction of temperature increase due to the RF-induced heating in a transmit array coil. (a) Induced flip angle under the tested B_1-shimming mode. (b) Predicted temperature change due to RF heating with the tested B_1-shimming mode in (a). (c) Measured temperature change using MR thermometry. Reproduced with permission from Zhang et al., Appl Phys Lett 2014; 105:244101.

TABLE I

Summary of MR accessibility of the different components of **B**

	Magnitude	**Phase**
B_1^+	"Direct" measurement	"Indirect" measurement
B_1^-	"Indirect" measurement	"Indirect" measurement
B_z	No measurement possible	No measurement possible